# Structured light manipulates material properties and reveals atomic changes in nanocrystals

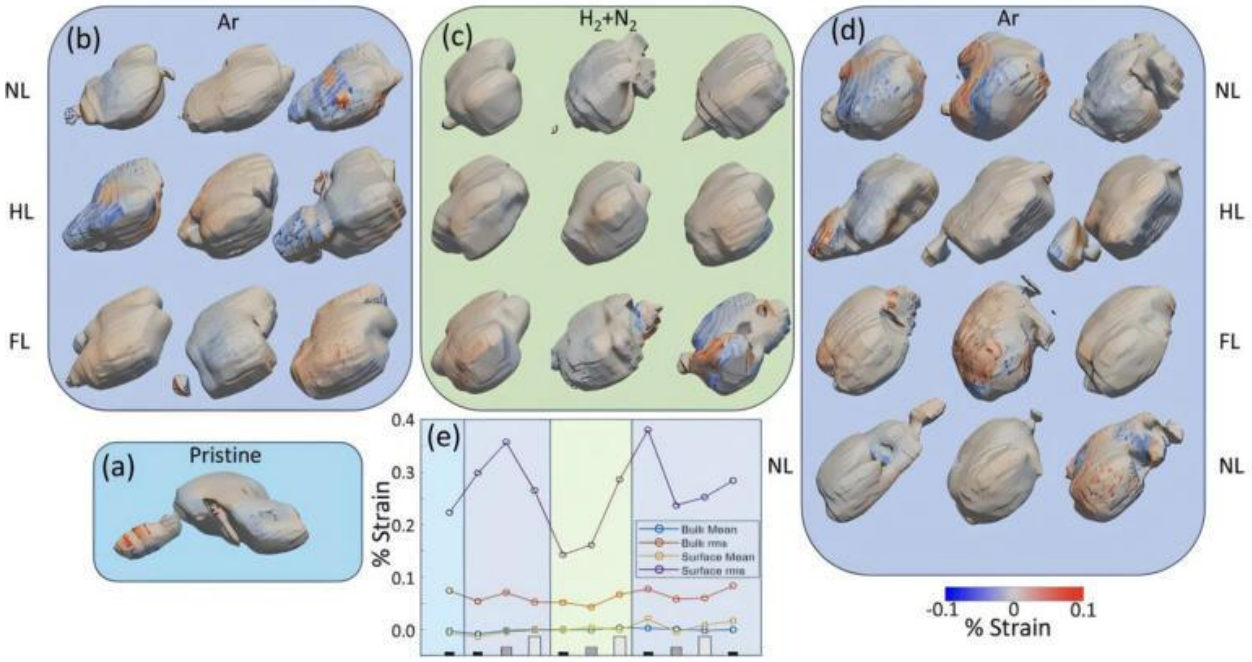


Visualization of strain and cracking in a bismuth tungstate nanoparticle under various environmental conditions. Credit: Advanced Materials (2025). DOI: 10.1002/adma.202504445

Researchers with the schools of science and engineering at Rensselaer Polytechnic Institute (RPI) are exploring new ways to manipulate matter with light to unlock a new generation of computer chips, photovoltaic cells and other advanced materials.

Physics professor Moussa N'Gom, Ph.D., and materials science professor Edwin Fohtung, Ph.D., have brought together their respective areas of expertise—optics and materials science—to illuminate previously unknown properties of the materials that will build the next generation of consumer, industrial and scientific devices.

"We can use almost the entire spectrum of light, from visible to X-ray, to manipulate and study materials," Fohtung said. "We can interrogate any system, from hard condensed matter to soft biological tissue."

Two of their findings, which explore how structured light can be used to alter and control material properties, were recently published in the journal *Advanced Materials* with the help of colleagues from RPI and Argonne National Laboratory.

In one of the papers, the researchers demonstrated that they can modulate the polarization of certain ferroelectric materials using light that has been "twisted," or given a spiral waveform. They found that this gives them a great deal of control over the internal polarization of the material.

"We often think of light photons like a hammer, striking down on a material to switch its polarization on or off," N'Gom said. "With this technique, however, we are using the photons more like a wrench: we can target a given set of atoms or ions in a crystal and manipulate the magnitude and configurations of the material's internal electric field."

They were able to capture detailed images of those manipulations using X-ray imaging. "The optical photons allow us to manipulate and form out-of-equilibrium configurations of the polarization textures, while the X-ray photons help us to capture three-dimensional images of the material's internal structure," Fohtung said.

It's a proof-of-concept for new classes of non-volatile ferroelectric random-access memory (FeRAM) devices, similar in construction to the magnetic dynamic random-access memory (DRAM) devices used in conventional electronics. FeRAM devices could enable more information to be stored more efficiently in the same amount of space.

"Everybody wants their devices to be smaller, faster, store more information and be more secure," Fohtung said. "We can do all those things with the method that we came up with. Using twisted light—light beams carrying orbital angular momentum (OAM)—to manipulate polarization textures represents a powerful, emerging strategy for designing FeRAM devices."

In the second paper, taking a major step forward for clean energy and materials design, a research team led by N'gom and Fohtung captured, for the first time, real-time 3D images of structural atomic changes inside individual nanocrystals as they react to heat, gases, and light.

Using a cutting-edge technique called Bragg Coherent Diffractive Imaging (BCDI), the team observed how bismuth tungstate ($Bi_2WO_6$) nanoflakes—materials widely explored for photocatalysis and solar-driven chemical reactions—change their internal shape, stress, and structure under realistic operating conditions. "It's like having X-ray vision into the heart of a single nanocrystal while it's working," Fohtung said.

This work overcomes a long-standing barrier in catalysis and energy materials: the inability to directly observe how single particles behave under real-world conditions. "These insights help us understand what drives performance—and failure—at the nanoscale," Fohtung explained. "That means we can design smarter, more efficient materials from the ground up."

In an experiment, the researchers found that exposure to intense light caused bismuth tungstate to break down, increasing the amount of surface area available to facilitate chemical interactions. They also found that the light could be used to induce a phase change in the catalyst from a metallic to a semiconducting state, effectively allowing them to switch the catalytic process on or off.

"Photocatalytic materials are significant for their unique capability to harness light energy to drive chemical reactions," N'Gom said. "This collaborative work aims to show that structured light can be employed to enhance their activity under visible light and to control their physical properties such as recombination of charge carriers, thereby improving overall efficiency."

"This work is a testament to the interdisciplinary nature of the research done at RPI, and to the creativity and inventiveness of our scholars," said Gyorgy Korniss, Professor and Head of RPI's Physics, Applied Physics and Astronomy department.

"Advanced imaging techniques not only provide incredible tools to probe fundamental properties of materials and living cells, but also pave the way for the development of new computer chips, memory storage units, and other advanced devices and materials that will make all of our lives better in the coming decades."

**More information:** Nimish P. Nazirkar et al, Manipulating Ferroelectric Topological Polar Structures with Twisted Light, *Advanced Materials* (2025). DOI: 10.1002/adma.202415231

Jackson Anderson et al, Real-Time Tracking of Nanoscale Morphology and Strain Evolution in $Bi_2WO_6$ via Operando Coherent X-Ray Imaging, *Advanced Materials* (2025). DOI: 10.1002/adma.202504445

Provided by Rensselaer Polytechnic Institute



# Manipulating Ferroelectric Topological Polar Structures with Twisted Light

Nimish P. Nazirkar, Viet Tran, Pascal Bassène, Atoumane Ndiaye, Julie Barringer, Jie Jiang, Wonsuk Cha, Ross Harder, Jian Shi, Moussa N'Gom, Edwin Fohtung
First published: 06 June 2025 **https://doi.org/10.1002/adma.202415231**

## Abstract

The dynamic control of non-equilibrium states represents a central challenge in condensed matter physics. While intense terahertz fields drive metal-insulator transitions and ferroelectricity via soft phonon modes, recent theory suggests that twisted light with orbital angular momentum (OAM) offers a distinct route to manipulate ferroelectric order and stabilize topological excitations including skyrmions, vortices, and Hopfions. Control of ferroelectric polarization in quasi-2D $CsBiNb_2O_7$ (CBNO) is demonstrated using non-resonant twisted ultra-violet (UV) light (375 nm, 800 THz). Combining in situ X-ray Bragg coherent diffractive imaging (BCDI), twisted optical Raman spectroscopy, and density functional theory (DFT), three-dimensional (3D) ionic displacements, strain fields, and polarization changes are resolved in single crystals. Operando measurements reveal light-induced strain hysteresis under twisted light–a hallmark of nonlinear, history-dependent ferroelastic switching driven by OAM. Discrete, irreversible domain transitions emerge as the topological charge $\ell$ is cycled, stabilizing non-trivial domain textures including vortex-antivortex pairs, Bloch/anti-Bloch points, and merons. These persist after OAM removal, indicating a memory effect. Competing mechanisms are discussed, including multiphoton absorption, strain-mediated polarization switching, and defect-wall interactions. The findings establish structured light as a tool for deterministic, reversible control of ferroic states, enabling optically reconfigurable non-volatile devices.

## Graphical Abstract

We demonstrate dynamic control of ferroelectric order in quasi-2D CsBiNb2O7 using twisted ultraviolet light carrying orbital angular momentum. Our approach harnesses non-resonant multiphoton absorption and induced strain to modulate topological of ferroelectric polarization

textures. In-situ X-ray coherent imaging and Raman spectroscopy reveal reversible, nanoscale polarization transitions, enabling efficient stabilization of topological solitons and paving the way for novel optoelectronic devices.


# 1 Introduction

In recent years, there has been a surge in condensed matter research toward nontrivial topologically-protected dipolar textures. These textures have predominantly been found in bulk materials, nanocrystals, and epitaxial heterostructures, where precise electrostatic, magnetostatic, and elastic boundary conditions are enforced on crystalline ferroelectric (FE) and magnetic materials. Since the prediction of flux-closure domain structures in magnetic films in the 1940s,[1, 2] parallels have been drawn in predicting and observing real-space topologically-protected dipolar textures such as flux-closures,[3] center domains,[4] vortices,[5, 6] skyrmions,[7] merons,[8] bubbles,[9] and hopfions[10] in ferroelectrics. These topological structures, especially in ferroelectric materials, hold potential for applications in high-density information storage, thin-film capacitors, actuators, and other electronic devices.[1, 2, 8] Furthermore, their inherent stability and rich interfacial phenomena offer promising avenues for multifunctional device architectures where electronic, magnetic, and mechanical responses can be synergistically exploited.

Advances in theory and experimental investigations have focused on the stabilization and observation of polar textures in ferroelectric systems. Studies have reported phenomena such as negative capacitance and the emergence of chirality in polar vortices and skyrmions, originating from sequences of achiral materials, using resonant soft X-ray diffraction-based circular dichroism and optical measurements.[11-14] Phase field simulations[15] and aberration-corrected scanning transmission electron microscopy have further shown that polar Bloch points (BPs) can be stabilized in substrate-induced tensile-strained ultrathin FE $PbTiO_3$ films. However, experimentally observing and manipulating these textures in a nondestructive and volumetric manner remains a significant challenge. Addressing these challenges is critical, as it would enable the precise control of domain architectures and the realization of devices with enhanced performance and novel functionalities.

In this work, we address these challenges by demonstrating the stabilization and manipulation of polar BPs in two-dimensional (2D) FE flakes using twisted light (TL) illumination and advanced imaging techniques. Specifically, the use of sub-band gap 375 nm twisted UV light enables

localized interactions with mid-gap states and multiphoton processes, dynamically modulating polarization textures and inducing strain inhomogeneities in free-standing $CsBiNb_2O_7$ (CBNO) flakes. Additionally, the nontrivial phase profile of TL allows for spatially resolved excitation, offering unprecedented control over the induced ferroelectric responses. By combining in situ X-ray Bragg coherent diffractive imaging (BCDI)[5, 16, 17] and optical Raman spectroscopy, we reconstruct 3D atomic displacements and strain maps, revealing reversible transitions from BPs to merons and back to BPs. Our observations advance the fundamental understanding of ferroelectric polar textures and open pathways for applications in next-generation spintronics technologies.

The microscopic origin of twisted UV light-induced strain heterogeneity in CBNO remains an open question, though several interrelated mechanisms are likely at play. Our observations suggest that non-linear optical processes–particularly multi-photon absorption facilitated by the structured wavefront of vortex beams–induce localized carrier generation, which perturbs the lattice and gives rise to strain patterns observed via Bragg Coherent Diffractive Imaging (BCDI) as shown in **Figure 1 d**. Additionally, selective sub-bandgap excitation of shallow defect states may couple to polar phonon modes, amplifying local distortions under twisted light.[18, 19] Strain-sensitive Rashba–Dresselhaus interactions also emerge as a crucial component, linking ferroelectric polarization, spin orbit coupling, and lattice deformations.[20-22] When TL with finite OAM impinges upon CBNO, it exerts a torque that influences the material's polarization state. Due to the strong spin orbit coupling (SOC) in this material, the OAM of the light can be effectively transferred to its spin texture, directly manipulating the spin states via the polarization texture. Consequently, the electronic band structure, including modifications in the Rashba spin splitting, can be dynamically tuned, enabling selective control over the spin texture. Furthermore, the handedness and magnitude of the OAM serve as additional degrees of freedom, allowing for deterministic tailoring of both polarization and spin configurations. This approach offers a dual control scheme in which the spatial (real-space) and momentum-space properties can be concurrently engineered.

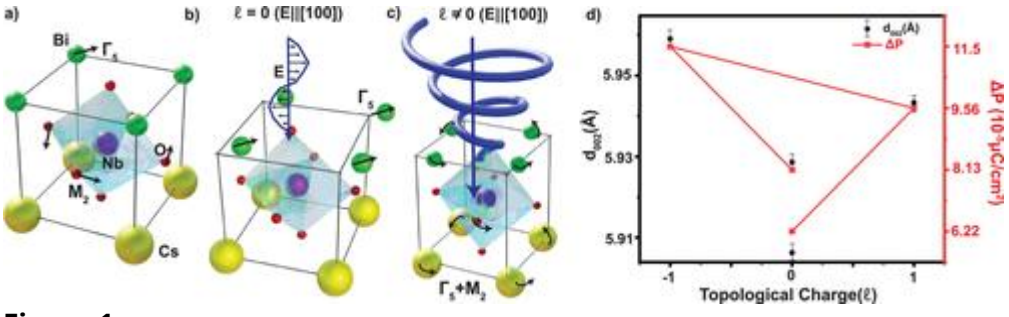


**Figure 1**

**Open in figure viewerPowerPoint**

Schematic of the manipulation of FE using vortex field from twisted light and its experimental detection. a) The $CsBiNb_2O_7$(CBNO) crystal unit responsible for FE, shown in the absence of twisted light. When driven by a plane-polarized 375 nm UV field in a Laguerre-Gaussian ($LG_\ell$) mode carrying orbital angular momentum (OAM) quantized at $\ell\hbar$ per photon, the twisted light interacts with mid-gap states and defect-mediated pathways through non-resonant mechanisms, inducing localized strain gradients and multiphoton absorption effects. This

interaction dynamically modulates ionic displacements and ferroelectric (FE) polarization textures. b,c) Twisted UV light topological charges $\ell = 0$ and $\ell \neq 0$ create quasi-static strain fields that couple to vibrational modes, driving polarization changes. b) Zone-center FE modes and c) zone-boundary octahedral tilting modes respond to the localized strain and OAM-induced torques, dynamically modulating the symmetry and polarization textures. d) Experimentally observed changes in polarization and atomic displacements along the [002] direction in CBNO arising due to the strain and phonon modes depicted in (b and c). These observations confirm that twisted UV light stabilizes non-equilibrium topological phases via defect-coupled and strain-mediated mechanisms.

By exploiting the interplay between Γ-point zone-center and M-point zone-boundary phonons, [20] we reveal phase transitions that stabilize polar vortex loops and $Z_2 \times Z_4$ topological textures in CBNO.

Our results demonstrate that TL can dynamically modulate ferroelectricity by transferring orbital angular momentum to induce ionic displacements and polarization changes, as illustrated in Figure **1**. The unique ability of TL to impart non-uniform electric fields and strain gradients without electrodes offers a transformative approach for studying and manipulating ferroelectric systems. These findings emphasize the role of sub-bandgap excitation pathways in driving polarization modulations and strain dynamics, paving the way for the development of ultrafast non-volatile memory switches and other optoelectronic devices. Overall, our work not only deepens the understanding of the intricate coupling between light and matter in ferroelectric systems but also sets the stage for future explorations into the integration of photonic and spintronic functionalities in advanced materials.

# 2 Results

To conduct the in situ TL BCDI experiment, we first synthesized free-standing CBNO 2D nanoflakes using a polymer precursor method.[23] These nanoflakes were then transferred onto the sample holder (see Experimental Section and Figures **S1** and **S2**, Supporting Information).

TL, also known as optical vortices or light carrying OAM, consists of electromagnetic fields[24, 25] with one or more singularities where the phase[24] is undefined, causing the intensity to vanish. The discovery of TL beams in visible light produced in free-space[24, 26] has generated significant interest across various scientific disciplines, including quantum information processing,[27] optical tweezers, super-resolution microscopy [28], and telecommunications.[29, 30]

**Figure 2c** illustrates exemplary phase and 2D intensity profiles (see Figures **S4** and **S31**, Supporting Information) in planes perpendicular to the propagation direction (*z*-direction) for the Laguerre-Gaussian ($LG_\ell$) mode of TL used in this experiment. LG beams are solutions to the paraxial wave equation,[24] and in the lowest order of the paraxial approximation, the electric and magnetic fields, as well as the vector potential, are purely transverse. Using the Lorenz gauge, the longitudinal component of the electric field (see Section **S7** and Figures **S4**– **S7**, Supporting Information) can be expressed in terms of a scalar potential as:

(1)

where $E_z$ is the longitudinal component of the electric field, Φ is the scalar potential, $c$ is the speed of light, $k$ is the wave number, ω is the angular frequency, $\mathbf{A}_0$ is the vector potential amplitude, $\nabla_\perp$ is the transverse gradient, and Π(**r**) is the complex amplitude of the LG beam, expressed as $\Pi(\mathbf{r}) = \Pi_0(r, z)\exp(i\ell\phi)$.

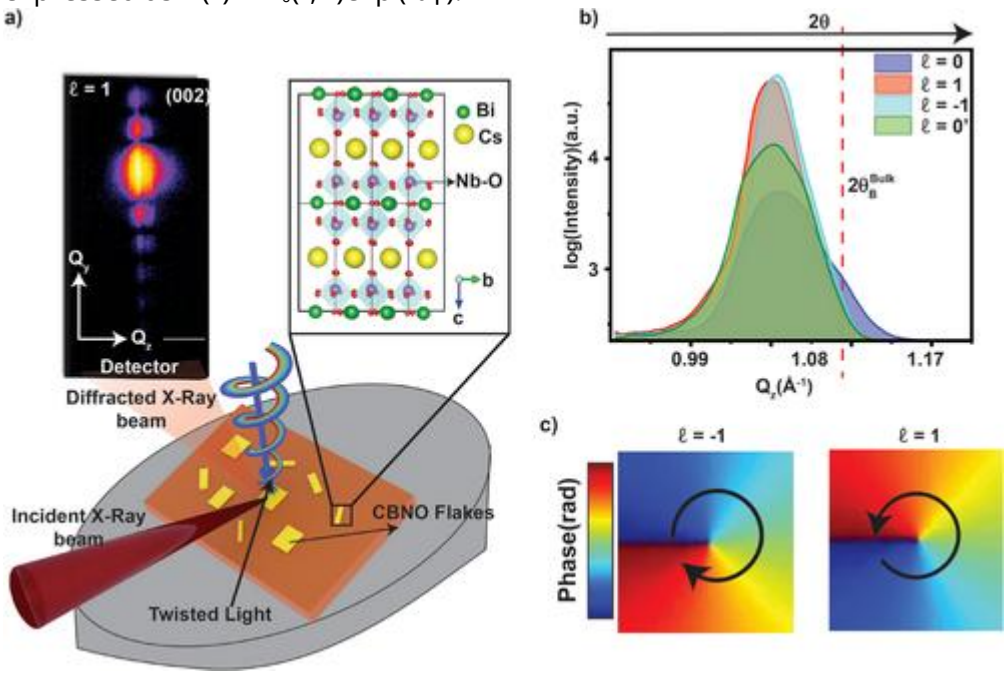


**Figure 2**

**Open in figure viewerPowerPoint**

In situ Bragg coherent diffractive imaging experiment. a) Coherent x-rays (red) are incident on a nanoflake (yellow) containing polarization vortices and FE domains subjected to twisted UV light (Red-yellow-blue) illumination. A schematic of a Dion-Jacobson layered oxide CBNO crystal which has been shown to harbor FE with high Curie temperature and large in-plane polarization is used as a model system to study twisted light control of atomic displacements, microscopic FE polarization and domain structure with near-atomic resolution observed as (b) shifts and broadening of the recorded Bragg peak intensity. Simulated phase of twisted UV lights with topological charges (ℓ) of 1 and −1, carrying OAM quantized in units of $\ell\hbar$ per photon (c). In our experiments, the diffracted X-rays collected at the detector plane carry information about the 3D electron density and atomic displacement fields within the nanoflake that allows us to monitor recorded X-ray intensity variations near the Bragg spot during a cyclical application of light topological charge from ℓ = 0, 1, −1, and back to 0.

In our in situ BCDI setup, we utilized a spatial light modulator (SLM) (more details in Experimental Section) to focus a 375 nm continuum (with constant beam power over time) of LG beams with varied topological charge ℓ normal to the in-plane direction ([100]-direction) of our CBNO sample (see Figure **1**). We generated a spatially inhomogeneous TL electric field $\mathbf{E}_{OAM}$ (**2**) and measured its intensity profile. For full derivation, see Figures **S4**– **S6** and Note **S7** (Supporting Information).

(2)

In Equation (**2**), $T$ is the time during which the CBNO nanoflake is under $LG_\ell$ beam illumination. At the time $t = 0$, we switched on the TL UV beam and, with the aid of the SLM and the neutral density filter, selected TL electric field polarization($\sigma = 0$) components $\mathbf{e}_x$ and $\mathbf{e}_y$ and magnitude such that $\mathbf{E}_{\|}[100]$ as shown in Figure **1**. We aligned the X-ray detector and CBNO crystal to satisfy the Bragg condition for the $d_{002}$ inter-atomic spacing of the (002) Bragg spot, as shown in **Figure 3**. For a duration $T$, we measured 3D diffraction near the (002) peak for beam topological charge $\ell = 0$. This procedure was repeated cyclically for $\ell = 0$, 1, −1, and back to 0 (see Figure **3a**). During the experiment, we observed TL-induced structural changes by tracking the characteristic asymmetrical behavior in diffraction patterns (see Figures **1b** and **3a**).

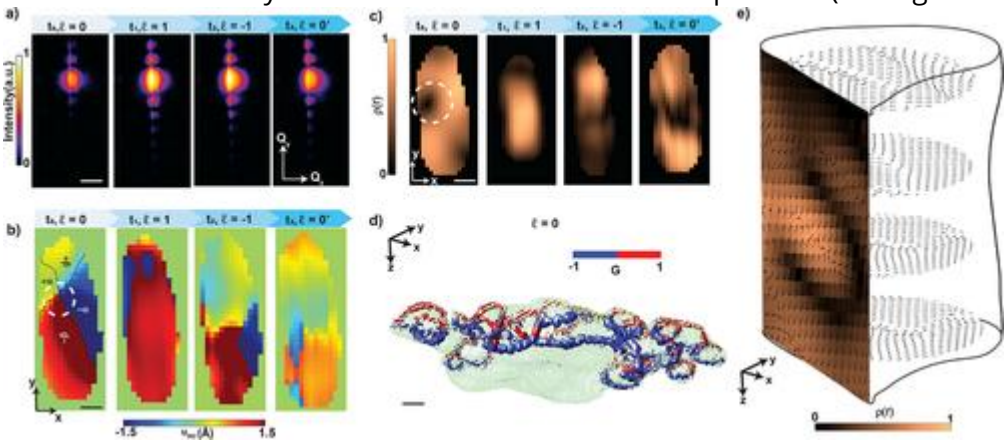

**Figure 3**

**Open in figure viewerPowerPoint**

Real-space topologically-protected polar structures under a vortex-light field. a) 2D slices from the recorded 3D coherent diffraction patterns for the (002) Bragg peak, used to measure the time evolution of the (b) FE displacement field during twisted light-induced structural changes. The polarization vortex core is identified at time $t_0$ under $LG_\ell$ beam illumination of $\ell = 0$ (zero OAM). As time progresses to $t_3$, changes in the displacement field are observed due to the nucleation of a vortex-antivortex pair. c) A 2D map showing the evolution of the central cut of a Bloch point in the freestanding CBNO. d) The magnitude of the toroidal moment density under $LG_\ell$ beam of $\ell = 0$. e) A rendering at time $t_0$ of CBNO under a TL electric field of $\ell = 0$, illustrating a vortex spanning the volume of the crystal along the $z$ −direction. Each cross-section perpendicular to the $z$ − direction contains a vortex texture, and the cut through the $y$ − direction shows a bloch-like behavior around the vortex core. The scale bar in (a) represents 0.01 $Å^{-1}$ while that in (b), (c), and (d) represents 60 nm.

X-rays scattered by a single CBNO nanoflake satisfying the (002) Bragg condition were recorded on an area detector (see Figure **3a**; and Section **S11**, Supporting Information). The experimental geometry, combined with the random orientation of the exfoliated nanoflakes, ensured that the (002) Bragg reflections from separate particles were well separated, allowing individual reflections to be isolated on the detector. The nanoflake was kept under continuous coherent TL UV illumination before the imaging experiment. From the coherent diffraction data, we reconstructed both the 3D distribution of the displacement field and the electron density ($\rho(x, y, z)$), along [002], $u_{002}(x, y, z)$, in an individual nanoflake with 14 nm spatial resolution (see Figures **S15**– **S17**, Supporting Information).

Figure **3b** shows a cross-section of the 3D displacement field [$u_{002}(x, y, z = z_0)$] in the FE nanoflake. The [002] direction is approximately along the $z$ −axis, while the X-ray beam is almost parallel to the $x$ −axis. Depending on the topological polar structure type, the angular distribution will have distinct features associated with a topological invariant known as the topological FE charge winding number:

(3)

This is a quantized value associated with FE defects such as vortices or skyrmions that measure the number of times the displacement vector field (or related order parameter) wraps around a given point or region in space. These topological features can influence the electronic properties and are important for applications in topological quantum computing and advanced electronic devices.[4, 6] In Equation (**3**) $A_i$ is the surface of a small volume containing the polar structure, $\epsilon_{ijk}$ is the Levi-Civita symbol, and  is the Born effective charge tensor component for atom κ, relating the $i$-th component of the polarization to the α-th component of the displacement of atom κ, obtained from DFT computations (see Experimental Section and Section **S9**, and Figures **S8**– **S11**) for the measured displacement field in Figure **3b**. Displacement fields generated by FE vortices are characterized by a winding number  around the vortex core in 2D (Section **S12**, Supporting Information), regardless of their polarity (clockwise or anticlockwise).[31] The angle  is related to the components of the displacement vector $\mathbf{u}_{002}(r)$. For polar BPs, the winding number captures the change in the displacement (polarization) direction in three dimensions. For anti-polar Bloch points (ABPs), the winding number captures the reversal in the polarization direction. The integral remains the same but yields a negative winding number due to the opposite orientation. Merons and anti-merons are characterized by half-integer winding numbers  and a discontinuous polarization field.

By inspecting Figure **3**, we identified topological polar structures such as vortices, merons, and BPs in the displacement field and electron density maps obtained by BCDI. Figure **3b** shows that at time $t_0$, two types of antiphase domains, α and β, can form in CBNO due to the presence of two bifurcation options. Combined with two possible in-plane polarization directions[23, 32] ("+" being parallel to the $a$ and $b$-axes and "−" being antiparallel to them), there are a total of four antiphase-FE $Z_2 \times Z_4$ domains (α +, β −, α −, and β +) existing in this system under $\ell = 0$ (see Figure **S18**, Supporting Information). Unlike trimerization observed in other improper FE materials such as the hexamanganites and hexaferrites,[33] where three-fold symmetric domains are formed, the transition in CBNO leads to an in-plane FE domain structure shown in Figure **3**.

In Figure **3b,d**, we qualitatively analyze the polarization vortex by inspection of the displacement field. Approximately 50 nm higher, in-plane Bi-ion displacement due to $LG_\ell$ electric field of $\ell = 0$ induces a periodic strain modulation (Figure **3**) in the $xy$ −plane above the vortex and creates tensile strain due to its larger lattice constant. However, approximately 50 nm below, the material compensates for this by creating a predominantly compressive strain with a smaller lattice constant. By looking at multiple planes above and below along the $c$ −direction, within the spatial resolution of the experiment, we corroborate this periodic modulation of tensile and compressive strain in the $xy$ −plane. The strain maps also show intersecting domains that form fork-like patterns in the $yz$ −plane. These fork-like features not only guarantee the formation of the vortices but also account for the observed polar BPs (Figure **3d,e**).

The magnitude of the $LG_\ell$ electric field for $\ell = 0$ is smaller than the reported coercive field[32] for CBNO (see Section **S7**, Table **S1**, and Figure **S6**, Supporting Information), thus explaining why we do not observe significant FE domain switching. To investigate how the observed strain modulation affects the FE polarization, we measured the relative shifts of α and β domains (Figures **S18** and **S19**, Supporting Information) under the TL induced electric field. We notice that at time $t_1$ under an OAM field of $\ell = 1$, the $\alpha^+$ and $\beta^+$ domains shift by vectors of 1/5[110] and −1/5[110], respectively, relative to the $\beta^-$. This corresponds to polar displacements as a result of $Bi^{3+}$ shift in the range of 0.25–0.6 Å, which is consistent with what is found in bulk CBNO.[23]

The evolution of the complex polar textures shown in the planar views of the CBNO displacement field and magnitude (Figure **3**) under the vortex electric field $\mathbf{E}_{OAM}$ can be better assessed by quantitative inspection of the three-dimensional BCDI reconstructions. Besides the winding number , we can describe the topological structure in terms of a non-zero toroidal moment,[8-10] defined as , where $\mathbf{P}_i$ is the local dipole moment located at $\mathbf{r}_i$ and $N$ is the number of dipoles (cells). $\mathbf{P}_i$ is estimated using the Born effective charge tensor, .

We compute the FE toroidal moment from the reconstructed polarization. Regions of the large toroidal moment are plotted in **Figure 4a**, where several 'tubes' and loops corresponding to the cores of vortices, antivortices, BPs, and ABPs are visible (see Figures **S24**– **S28**, Supporting Information). Unlike in incompressible fluids, where the divergence must vanish, a non-zero divergence of the FE polarization due to complex topological structures like FE vortices and BPs signifies the presence of bound charges that play a role in the formation and stability of these structures under the TL-induced vortex field. BPs and ABPs are identified by positive (red) and negative (blue) values within the reconstructed toroidal moment field. We observe a large number of 3D loops (Figure **4a**) that resemble vortex rings under $LG_\ell$ electric field of $\ell = 1$. We consider the case of one such loop, identified by plotting an isosurface corresponding to a maximum threshold of $\pm 0.05 P_s$ (Figure **4a**). This loop is located in the vicinity of a single Bloch (anti-Bloch) point, spanning a region of the CBNO crystal. This loop texture represents a departure from the coaxial string-like topology observed under the TL-induced vortex field of $\ell = 0$ and $\ell = 1$ (Figures **S26**– **S28**, Supporting Information). The 2D cut planes in Figure **4b** show the vector field of change in $P_{mag}$ (see Section **S16**, Supporting Information), allowing us to identify topological features such as head-to-head convergence, tail-to-tail divergence, BPs, ABPs, and merons.

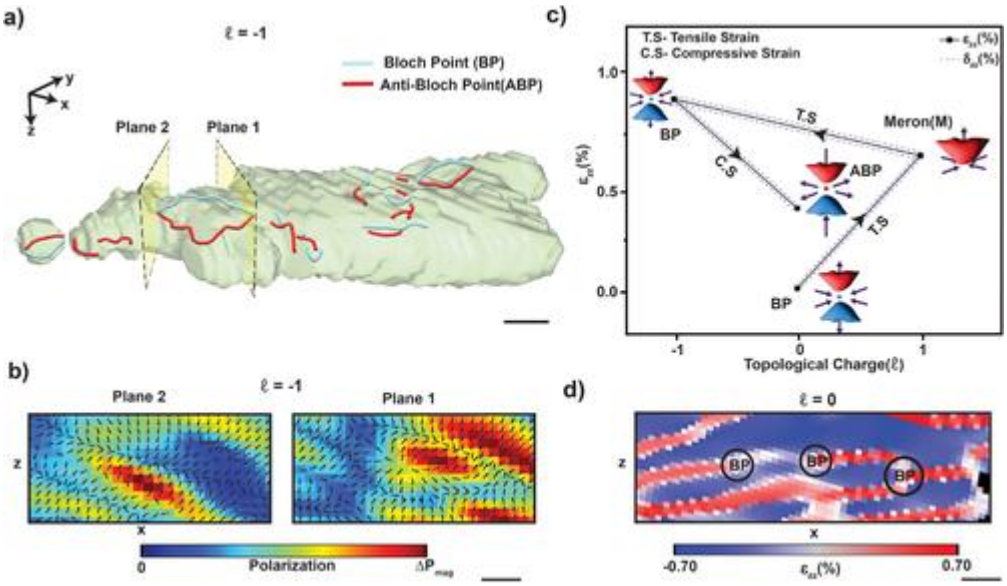


**Figure 4**

**Open in figure viewerPowerPoint**

Twisted light-induced polar Bloch point transitions and strain evolution. a) BCDI rendering of the magnitude of the toroidal moment density under OAM of ℓ = −1, capturing the topology formed by Bloch and anti-Bloch points. b) 2D slices depicting the density of BPs and ABPs in the toroidal field, marked by planes in (a), with the normalized magnitude of polarization $\Delta P_{mag}$vectors overlaid. c) Hysteresis-like loop capturing OAM field-induced strain $\epsilon_{zz}$ and BP transition states in CBNO. d) BCDI strain map under an OAM field of ℓ = 0 showing that BPs are associated with regions of reduced polarization magnitude or significant strain gradients. Scale bars correspond to 100 nm.

In Ref. [**15**], polar BPs were observed in strained $PbTiO_3$ films using phase-field simulations and aberration-corrected scanning transmission electron microscopy at the locations where a vortex core intersected a domain wall. Similarly, we find that the BP pair is located at the intersection of the vortex-antivortex loop with a domain wall separating regions of opposite strain magnitude (Figure **4d**). It was predicted in the same reference that polar BPs can be stabilized using substrate-induced tensile strain in FE films. In Ref. [**31**], a periodic shear strain landscape was generated by stacking freestanding FE perovskite layers with controlled twist angles, akin to Moiré lattices.[34] An important remark is that in both cases above, the inter-layer strain in the film cannot be dynamically tuned.

Here, in Figure **4c**, we observe that under $LG_\ell$ electric field transitioning from ℓ = 0 to ℓ = 1, then ℓ = −1, and back to ℓ = 0, we can manipulate the global and local strain within the CBNO crystal in a controllable manner (Figures **S19** and **S21**, Supporting Information). Under a global tensile strain $\varepsilon_{zz}$ of 0.7%, there is a transition from BPs to merons. A slight increase in the tensile strain to $\varepsilon_{zz}$ of 0.75%, by changing the vortex field to ℓ = −1, reverts to a global Bloch point state. Subsequent compressive strain back to ℓ = 0 transitions to a global ABP state within the CBNO crystal (Tables **S2** and **S3** and Figure **S23**, Supporting Information). Figure **S20** (Supporting Information) shows the local mapping of the strain modulations and induced shear strains that mediate the observed BP transitions. It is worth noting that such controlled strain manipulation

and the observed strain landscape are unique, as they cannot be attained, to the best of our knowledge, either by epitaxial strain or by any pattern of externally applied stresses or electrodes.

In Figures **3** and **4**, we have presented experimental evidence of the formation of polar topological states in the quasi-2D FE nanoflake, with emerging polarization vortex structures that are axially symmetric at time $t_0$ under $LG_\ell$ electric field of $\ell = 0$. However, the creation of a vortex costs additional energy due to the existence of the vortex core where the FE is suppressed. Thus, under UV $LG_\ell$ beam illumination of $\ell = 1$, the singularity at the vortex core can be completely eliminated by the escape of the vector field into the third dimension (see Figure **S20**, Supporting Information) along the vortex axis, leading to the emergence of chiral meron-like structures in the flake. Under TL illumination of $\ell = -1$, the system returns to a BP state, while subsequent compressive strain allows the polar structure to transition to an ABP state under a TL-induced $LG_\ell$ field of $\ell = 1$.

In addition to the observed TL-induced OAM field-induced strain and manipulation of real-space FE polar structures from BCDI, OAM-dependent Raman measurements on CBNO suggest a possible correlation with twisted UV light-induced excitation of the zone-center and zone-boundary modes in CBNO (see details in Experimental Section and Figures **S9**, **S10** and **S12**, Supporting Information).

**Figure 5a** illustrates the experimental setup for OAM-dependent Raman measurements on CBNO. Details of the experimental methodology can be found in Experimental Section. A reference scan was initially performed to confirm the unperturbed crystal structure of CBNO, as shown in Figure **S30** (Supporting Information). Subsequent Raman scans were conducted under various OAM conditions, similar to BCDI measurements ($\ell = 0$, $\ell = 1$, $\ell = -1$, and returning to $\ell = 0$). We monitored both the in-plane zone-center phonon mode, reported around 190 $cm^{-1}$ for the Bi-O bond,[35] and the out-of-plane phonon mode, as depicted in Figures **5d,c**, respectively. Illumination with $\ell = 0$ resulted in tensile strain along the c-axis, while the OAM field with $\ell = 1$ induced a compressive effect. These findings are consistent with the BCDI measurements. A reversible behavior was observed with $\ell = -1$, and returning to $\ell = 0$ resulted in a Raman spectral shift that matched the initial state. This reversibility was also seen in the zone-boundary phonon mode, which has been reported around 580 $cm^{-1}$ for the Nb-O in-plane Raman peak,[36] as shown in Figure **5b**. The consistent nature of these trends was confirmed by tracking the Raman peak position at full width at half maximum (FWHM), as illustrated in Figure **5e**.

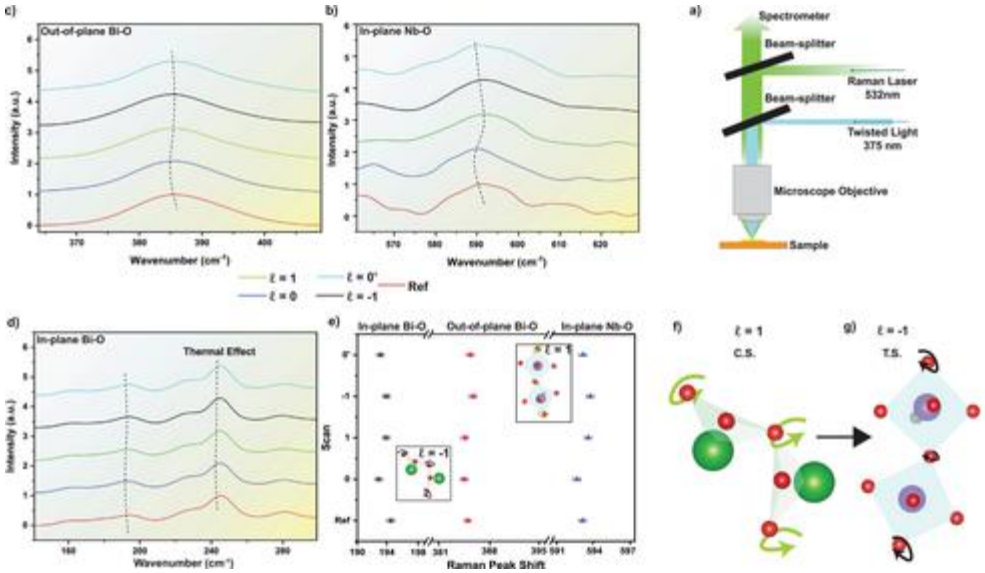


**Figure 5**

**Open in figure viewerPowerPoint**

Twisted-light dependent Raman spectroscopy on CBNO: a) Schematic of the in situ Raman experimental setup designed to probe photo-induced structural changes, modulation of phonon modes, and domain dynamics in a CBNO nanoflake under $LG_\ell$ light illumination. The setup utilizes a 532 nm Raman laser with a 375 nm coherent twisted light of varying topological charges. b) Line plots showing the behavior of the out-of-plane phonon mode for the Bi-O layer. The spectra demonstrate reversible shifts in peak positions, characterized by a tensile shift from the reference to $\ell = 0$, compression under $\ell = 1$, and a reversion to a tensile state under $\ell = -1$, with minimal changes upon returning to $\ell = 0$. This suggests significant OAM-induced modulation of vibrational states. c) Line plots illustrating the out-of-plane phonon modes of the Bi-O layer, including isolated Bi atom responses. The plots indicate compression effects attributed to thermal influences from continuous illumination, highlighting the sensitivity of Bi phonon modes to UV $LG_\ell$ light and thermal input. d) Line plots for the in-plane phonon modes of the Bi-O layers, showing reversible Raman peak shifts similar to those observed in the out-of-plane Bi-O modes, underscoring the symmetric impact of OAM on in-plane Bi-O vibrations. e) Summary of Raman peak shifts across different modes when interacting with twisted light carrying various topological charges. Insets depict the structural and bond modifications along with torsional strain effects induced by twisted light, demonstrating the impact of OAM on lattice dynamics (refer to Figures **S10**, **S13**, **S32**, and **S33** and Table **S4**, Supporting Information for detailed analysis). f–g) Schematic representations of interactions between twisted light with topological charges $\ell = 1$ (Compressive Strain) and $\ell = -1$ (Tensile Strain), with Bi-O tetrahedra and Nb-O octahedra, respectively. These illustrate the torsional and structural changes imparted by non-zero OAM, contributing to the understanding of vortex-light-induced Raman activity.

Schematics showing the effects of twisted light (TL)-induced OAM fields ($\ell = 1$ and $\ell = -1$) on the Bi-O and Nb-O bonds are presented in Figure **5f,g**, respectively. The schematic is inspired by the data shown in Figures **5b–d**, where we observe a reversible tensile and compressive behavior in strain in the phonon modes. This reiterates and emphasizes the ability of the TL-induced

electric fields to control the bending and breathing of the phonon modes in the nanocrystal. An inset illustrating the inverse case is shown in Figure **5e**, and a detailed analysis of the shifts in polarization is depicted in Figure **S9** (Supporting Information). The Raman spectroscopy results align with the proposed interaction mechanism between TL and FE polarization in CBNO. Qualitatively, comparisons between BCDI and Raman spectroscopy reveal a hysteresis-like behavior in both strain and Raman peak shifts. This is analogous to the traditional hysteresis observed between polarization and electric field in FEs, where the beam topological charge acts similarly to a variable electric field. However, the complex nature of the $LG_{\ell}$ electric field provide a wider space to manipulate the sample. This demonstrates the potential for controlling FE topologies using TL, opening new avenues for research into vortex-light–matter interactions.

We propose that the interaction mechanism involves the coupling of TL with the electronic structure, leading to shifts in phonon modes within the CBNO nanoflake. One potential interaction mechanism is intra-band transitions, as discussed in Sections **S8** and **S10** (Supporting Information). We suggest that electron-mediated shifts in the phonon mode structure result in the observed changes in strain, where a preferential shift in the electronic structure is noted (see Figure **S14**, Supporting Information) within the tight-binding approximation of the CBNO band structure. In both BCDI and Raman spectroscopy experimental techniques, the effects are observed post electron–phonon renormalization, leading to the observed Raman peak shifts, FE polarization, and strain behavior. A thermal effect is shown in Figure **5d**. The wavenumber relates to Raman frequency shifts in the Cs-O bonds. However, Cs does not contribute to the ferroelectric landscape of CBNO. This thermal effect also helps us isolate the effect of a thermal energy induced shifts and the shifts induced by the orbital angular momentum of the TL on the ferroelectric behavior of the system.

Our experimental results, supported by theoretical analysis, reveal that the OAM states $\ell = 0$ and $\ell = 0'$ correspond to a uniform electric field distribution, while $\ell = 1$ and $\ell = -1$ result in a non-uniform electric field when illuminating the nanoflake. In both cases, the strength and direction of the electric field vary depending on the beam waist and the topological charge. Under a homogeneous electric field corresponding to $\ell = 0$, a stable 2D vortex structure was observed at time $t = 0$, with the vortex core aligned along one of the crystallographic axes [001] (see Figure **3c**). A small quasi-static field applied at $t = 0$ stabilized an axial vortex core, which is topologically protected by two antiphase nanodomains with nearly homogeneous spontaneous polarization (see Section **S8** and Figure **S22**, Supporting Information).

Similar to ferromagnetic vortices, the core of the observed ferroelectric vortex behaves like a dipole, offering the potential to rotate the vortex axis under the influence of a small quasi-static electric field, whether homogeneous or inhomogeneous. Due to strong ferroelectric anisotropy, which hinders the rotation of the dipolar vortex core and tends to align it along one of the crystallographic directions, the orientation of the core in the field is determined by the minimization of dipolar and anisotropy energies. As the vortex core is coupled to the antiphase domains, the plane of the vortex, which is perpendicular to the core axis, can rotate along with the core. The core size is sensitive to variations in the TL-induced electric field, and as these variations occur, the nanoflake gradually transitions toward a single-domain state, as observed at time $t = t_1$.

Manipulating FE polarization in quasi-2D materials like CBNO using incident vortex fields generated by coherent twisted ultraviolet light offers distinct advantages over using pulsed terahertz infrared photons, as traditionally employed in 3D perovskite materials like $SrTiO_3$. Twisted ultraviolet light carries topological charge, imparting angular momentum to the electrons and ions in the material, leading to precise interactions with ferroelectric polarization. This helical phase can stabilize transitions between Bloch points and merons by aligning polarization vectors and modifying the energy landscape, thereby lowering the energy barriers for these transitions. The higher spatial precision and photon energy of UV light allow for more effective and localized polarization changes compared to terahertz infrared pulses. Additionally, vortex fields carrying orbital angular momentum can selectively interact with specific phonon modes or electronic states that are not easily accessible with terahertz infrared pulses, providing a unique tool for manipulating ferroelectric polarization.

In 3D perovskite oxides systems,[37-39] pulsed terahertz infrared photons can resonantly excite specific phonon modes, inducing transient changes in ferroelectric polarization and numerous emergent phenomena.[40-42] However, the additional degree of freedom and increased pathways for energy dissipation in 3D systems make it more challenging to achieve the same level of control and precision as in quasi-2D systems. Therefore, using electric field of coherent twisted ultraviolet light to manipulate ferroelectric polarization in quasi-2D CBNO provides superior control and effectiveness, enabling the stabilization of complex topological transitions.

## 2.1 Observed Strain Hysteresis

Figures **1d** and **4c** provide clear experimental evidence of strain hysteresis in CBNO under twisted light illumination. This hysteresis is a hallmark of nonlinear, history-dependent ferroelastic domain dynamics induced by the orbital angular momentum (OAM) of the light field.

The observed strain hysteresis suggests discrete, irreversible domain switching events in response to varying OAM topological charge $\ell$. As in conventional ferroelectric polarization-field hysteresis, this behavior implies the nucleation, reorientation, and stabilization of non-trivial domain configurations (e.g., Bloch points, vortex-antivortex pairs) which do not fully relax when $\ell$ is reduced. Additionally, domain wall pinning by intrinsic defects or impurities likely enhances this lagged response, contributing to the observed memory effect.

The coupling between TL and FE polarization creates a complex energy landscape with multiple metastable states separated by energy barriers. This energy profile results in different structural pathways during the increasing and decreasing $\ell$ cycles, producing the characteristic hysteresis loop. The behavior is consistent with first-order-like phase transition dynamics, where switching between distinct strain or polarization states is discontinuous and strongly path-dependent.

The spatial phase profile of TL, characterized by the topological charge $\ell$, introduces an inhomogeneous driving force on the lattice. This optical torque modulates the strain state in a non-single-valued manner, leading to hysteresis in the strain response. Furthermore, local

lattice distortions generated by photoinduced effects persist beyond the duration of the applied OAM, suggesting slow relaxation dynamics or trapping in metastable states.

This observed strain hysteresis – with its strong dependence on the history of applied $\ell$ – demonstrates the potential for OAM light to induce non-volatile strain states in ferroelectric materials. Such memory effects are attractive for reconfigurable photonic, straintronic, and non-volatile memory applications. Future pump-probe BCDI or ultrafast Raman studies could provide time-resolved insights into the domain switching and relaxation processes, while theoretical modeling using Landau-Ginzburg approaches incorporating OAM coupling terms may capture the underlying energy landscape and switching dynamics.

## 2.2 Alienating Thermal Effects

The strain and polarization changes induced by TL are qualitatively distinct from conventional thermal effects. Temperature-dependent Raman measurements on the Nb–O vibrational modes display a monotonic, linear shift with increasing temperature, consistent with thermal expansion or phonon softening(see Figure **S35**, Supporting Information). In contrast, under TL illumination, the Raman modes exhibit cyclical, hysteresis-like behavior as the topological charge $\ell$ is varied between −1, 0, and +1 – a signature of complex, history-dependent domain reconfiguration rather than continuous heating effects.

Complementary BCDI measurements further corroborate this interpretation, revealing spatially localized lattice distortions and domain rearrangements that correlate with the applied OAM of the vortex beam. Given the moderate laser power density and the limited penetration depth of 375~nm light in CBNO, significant bulk heating is unlikely. Overall, the combined Raman and BCDI evidence confirms that the observed strain hysteresis originates from intrinsic OAM-induced ferroelastic phenomena rather than trivial laser-induced thermal effects.

## 2.3 Mechanism of Twisted Light-Induced Strain

At this stage, it is not quite obvious from the exact microscopic mechanism responsible for twisted UV light induced strains. We shall address a few possibilities.

### 2.3.1 Non-Linear Optical Processes

In our investigations, the microscopic mechanisms responsible for TL-induced strain heterogeneity in CBNO could be potentially attributed to the interplay between non-linear optical processes and spatial phase modulation of the incident vortex beam. Although the UV excitation (375 nm, ≈3.31 eV) is slightly below the measured bandgap of CBNO (3.64 eV), the wavefront-shaping, and structured electromagnetic fields provided by the TL facilitate multi-photon absorption. This multi-photon process may lead to the generation of photoexcited carriers that locally perturb the crystal lattice, giving rise to heterogeneous strain fields observed by BCDI (see Figures **3** and **4**). Also, experimental observations–such as intensity/power-dependentsee (see Section **S19** and Figure **S37**, Supporting Information) non-

linear shifts in Raman modes (notably the Nb–O vibrational mode) and spatially resolved lattice distortions via BCDI–lend support to the contention that non-linear absorption processes[18, 19] are pivotal in realizing these strain heterogeneities.

Moreover, the formation of head-to-head and tail-to-tail domain walls, as well as BPs, suggests that charge screening plays a critical role in the overall mechanism. In the non-linear screening regime, the photoexcited electron–hole pairs effectively screen the spontaneous polarization through mechanisms where the screening energy is intrinsically proportional to the electronic bandgap. Such interplay between charge screening and strain has parallels with the fast photostrictive responses observed in ferroelectric materials, where the rapid, local strain induced by light is notably non-thermal in nature.[43]

Moreover, the formation of head-to-head and tail-to-tail domain walls observed in our BCDI results, as well as BPs, suggests that charge screening plays a critical role[44] In the non-linear screening regime, the photoexcited electron–hole pairs effectively screen the spontaneous polarization through mechanisms in which the screening energy is proportional to the electronic bandgap. Concurrently, the unique spatial phase and orbital angular momentum associated with twisted light can potentially introduce a chiral component to the excitation process. This aspect can further modulates the local electronic structure and reinforces strain heterogeneity via selection rules that permit non-dipolar transitions.[45] This scenario is further substantiated by studies demonstrating that the OAM inherent in twisted light facilitates interaction pathways leading to hyper-Raman and hyper-Rayleigh responses, underscoring the role of non-linear optical susceptibility in complex materials.[45, 46]

In combination, these effects provide a robust framework for understanding how multi-photon absorption, modulated by the vortex beam's spatial structure, induces complex domain dynamics and strain patterns in CBNO.

## 2.3.2 Rashba–Dresselhaus Effects

In addition to the non-linear excitation pathways, the formation of domain walls with accompanying BPs/ABPs indicates that charge screening plays a critical role. The screening of spontaneous polarization in ferroelectrics such as CBNO is achieved when generated electron–hole pairs provide sufficient compensation for the intrinsic polarization field–a process that is energetically linked to the electronic bandgap.[47]

Recent theoretical studies[20, 21] on Rashba–Dresselhaus FE CBNO have highlighted the intimate coupling between its FE polarization and strong spin–orbit interactions and strain.[22] In the FE state of CBNO, the absence of inversion symmetry leads to pronounced Rashba spin splitting, which is highly sensitive to strain. Mechanical strain alters local lattice parameters and modulates the ferroelectric polarization, thereby changing the internal electric fields that govern the Rashba effect.

Both tensile and compressive strains (see Figure **4**) doesn't only manipulate the texture of FE polarization but can tune the band structure of CBNO, affecting not only the bandgap but also

the magnitude of the spin splitting. This strain-induced modulation provides a powerful avenue for engineering persistent spin helix states,[48] which are critical for low-power spintronic applications. Moreover, the interplay between strain, complex domain configurations (such as head-to-head and tail-to-tail domain walls and BPs), and TL excitation leads to non-linear screening effects that manifest through the generation of electron–hole pairs to fully screen the spontaneous polarization. Since the screening energy is proportional to the electronic bandgap, these findings underscore the potential of CBNO as a platform for dynamically tuning both its electronic and spintronic properties.

Overall, we suggest that the interplay between non-linear optical processes–including multi-photon absorption–and the spatially varying phase profile of the vortex beam can be central to the observed phenomena. The electromagnetic fields of the twisted light induce non-linear polarization effects in the CBNO crystal, can enhance the generation of photoexcited carriers. These carriers modify the local lattice screening and electronic distribution, leading to heterogeneous strain fields that are further reinforced by the spatial modulation of the vortex beam. Although direct, microscopic validation of each individual process remains challenging, the combined evidence from Raman spectroscopy, BCDI, and intensity studies provides plausible support for these non-linear effects as possible drivers of the strain heterogeneity and domain dynamics observed in our experiments.

## 2.4 Selective Coupling to Polar Phonon Modes Via Sub-Bandgap Excitation in CBNO:

In CBNO, the 375 nm UV excitation (approximately 3.31 eV) is slightly below the measured bandgap of 3.64 eV (see Figure **S12**, Supporting Information). Under these sub-bandgap conditions, photons can selectively excite shallow defect states that reside within the bandgap. These defect states, when populated, interact with the lattice via electron–phonon coupling, particularly influencing the polar phonon modes that are highly sensitive to local charge distributions. The excitation of these shallow defect states leads to localized modulation of the polar phonon modes, resulting in spatially inhomogeneous lattice distortions. Under the influence of twisted light, with its unique spatial phase and high intensity, these localized effects are further amplified, ultimately giving rise to the observed strain heterogeneities in CBNO.

This mechanism involves an initial sub-bandgap excitation of defect states, which then couple selectively to polar phonon modes, modifying the local ferroelectric polarization and creating regions of differential strain. Future studies could confirm this mechanism by employing time-resolved Raman spectroscopy and pump–probe techniques to monitor the dynamics of defect state excitation and their influence on polar phonon modes. Moreover, theoretical models that incorporate electron–phonon coupling under twisted-light excitation, alongside spatially resolved measurements such as scanning probe microscopy under in situ illumination, would provide further insights into the selective modulation of polar modes and the resulting strain distributions.

To further elucidate the exact microscopic mechanisms at play in CBNO under TL excitation, several experiments can be envisaged. Time-resolved TL pump–probe measurements, such as ultrafast BCDI and time-resolved Raman spectroscopy, would allow us to capture the dynamics of photoexcited carrier generation, lattice distortion, and domain wall motion on ultrafast timescales. Systematic intensity-dependent studies, where the incident light intensity and topological charge are varied, could help distinguish threshold behavior associated with multi-photon absorption from linear optical responses. Complementary temperature-dependent experiments would further aid in decoupling thermal effects from intrinsic non-linear optical phenomena. Additionally, non-linear optical techniques like twisted-light second-harmonic generation (SHG) could provide direct insights into the evolution of the polarization state, while time-resolved angle-resolved photoemission spectroscopy (TR-ARPES) might reveal modifications in the band structure and Rashba spin splitting induced by twisted light. Finally, spatially resolved measurements using scanning probe techniques such as piezoresponse force microscopy (PFM) under in-situ illumination could map ferroelectric domain dynamics and clarify the role of head-to-head and tail-to-tail domain walls, as well as Bloch points, in charge screening. Collectively, these experimental approaches would offer a comprehensive understanding of the interplay between non-linear absorption, charge screening, and domain dynamics in CBNO.

# 3 Conclusion and Outlook

We have demonstrated that the orbital angular momentum electric field from twisted light can dynamically induce strains (both tensile and compressive) up to ≈0.8% along the c-axis in individual quasi-2D ferroelectric CBNO crystals. These strains are quantifiable, with nanometer resolution, and can be controlled reversibly, creating significant strain gradients. However, we observed irreversibility in some strain states, particularly during cycling of the topological charge (ℓ) of twisted light. This irreversibility resembles hysteresis-like behavior, which could arise from defect pinning, localized energy barriers, or strain-induced polarization switching. A deeper investigation into this hysteresis effect is required, including systematic hysteresis loop measurements to fully characterize the coupling mechanism. This phenomenon is potentially universal to quasi-2D ferroelectric systems with weak out-of-plane bonding along the stacking direction. For example, in CBNO, the reported piezoelectric coefficient $d_{33}$ (8 pC $N^{-1}$)[49] is significantly smaller than in typical 3D perovskite oxides (e.g., $PbTiO_3$, $BaTiO_3$,[50] $BiFeO_3$). Our observations show that topologically protected polar structures and transitions from Bloch points to merons occur under a light-carrying orbital angular momentum electric field, mediated by induced tensile strains. These findings align with earlier reports of polar Bloch points in strained epitaxial thin films. However, in epitaxial thin films, the mechanical boundary conditions are rigid and determined by the atom-on-atom replication of the substrate structure, leaving little room for modification. Additionally, reversible and dynamic control of torsional, shear, or inhomogeneous strain patterns is not easily achievable via epitaxy.

In summary, we have found that it is possible to induce non-trivial ferroelectric textures and polar structures, as well as strains in quasi-2D freestanding ferroelectric crystalline flakes. The coupling mechanism involves the twisted light's spatially varying electric field interacting with

the material's polarization and strain fields, leading to localized ionic displacements and quasi-static strain gradients. These couplings not only drive the nucleation of vortex-like and Bloch-type modulations but also create persistent, field-driven strain profiles that may depend on the specific topological charge (ℓ) of the light. This interplay between the electric field gradients, defects, and polarization states underpins the hysteresis-like effects observed in our experiments. Furthermore, the nature of these 2D and 3D topological structures can be largely tuned by controlling the twisted light's topological charge.

Moreover, the interaction of twisted light with ferroelectrics potentially opens new avenues for research into the dynamical twist-multiferroics[42] and the braiding of polar 1D structures. To further explore these phenomena, a full hysteresis loop measurement and time-resolved techniques are necessary to resolve the dynamic behavior of polarization and strain under varying ℓ. Additionally, combining twisted UV light with other modalities, such as higher-order Bessel beams or circularly polarized twisted light, could uncover new mechanisms of light-matter interaction. Upgrades in the coherence[51, 52] of synchrotrons and the development of time-resolved orbital angular momentum pump orbital angular momentum-probe Bragg coherent diffractive imaging techniques that require twisted X-rays[53] could potentially provide deeper insights into the dynamical control of novel states of matter that are unattainable by conventional thermodynamic methods. Additionally, the development of new Bragg coherent diffractive imaging methods to access in-plane strain and orbital angular momentum-dependent Raman spectroscopy to capture chiral or more nuanced twisted-light interactions could represent a paradigm shift in engineering beyond 2D. These advances would not only enhance the understanding of twisted-light interactions but also open possibilities for designing multifunctional devices, where ferroelectric and multiferroic states can be dynamically controlled in real-time. This includes the potential for dynamical manipulation of the twist angle in which other modes of twisted light, such as higher-order Bessel beams with higher penetration, could play important roles. Shedding further light on these advances would be a great challenge, for both theory and experiment, but is beyond the scope of the present work.

In the near future, combining twisted light with experimental techniques such as angle-resolved photoemission spectroscopy (ARPES) and high-harmonic generation (HHG) will serve as promising tools for probing these reported interactions. ARPES can be used to monitor changes in the spin texture, while HHG can generate attosecond pulses carrying OAM for ultrafast manipulation of the spin states. This dual capability of controlling both real-space polarization and momentum-space spin texture represents a significant advancement in the field of spintronics, with profound implications for next-generation memory devices, quantum computing, and other applications requiring precise spin current control.

# 4 Experimental Section

## Fabrication of Freestanding Quazi-2D Flakes

Free-standing CBNO 2D flakes were synthesized using a molten-salt assisted method.[23, 36] Further, pre-characterization was carried out to confirm the stoichiometry using

XPS (Section **S4** and Figure **S2a**, Supporting Information), morphology using XRD and SEM (Sections **S2** and **S3** and Figure **S1**, Supporting Information) and bandgap using transmission spectroscopy (Section **S5** and Figure **S2b**, Supporting Information). Stability measurements were also performed under excitation with UV light with gaussian profile and timed raman measurements were taken for 120 mins as shown in Figures **S34** and **S38** (Supporting Information).

## Twisted Light Bragg Coherent Diffractive Imaging Experiments

The Si (111) monochromator at the Advanced Photon Source's sector 34-ID-C was utilized to isolate coherent X-ray photons with an energy of 9.0 keV. The beam's monochromaticity was defined by an energy bandwidth of 1 eV, and it exhibited a 0.7 μm transverse coherence length. The X-ray beam was focused onto the sample using a pair of Kirkpatrick-Baez mirrors situated after the beam-defining aperture. For this experiment, the beam size was set to 700 by 700 nm. The principle of the Bragg coherent diffraction experiment was illustrated in Figure **S3** (Supporting Information). A Medipix2 CMOS X-ray detector was positioned around the diffraction sphere using a motorized arm. The detector was aligned with the outgoing (002) characteristic Bragg reflection from the CBNO sample. To magnify the interference fringes in the diffraction pattern, the detector was placed 1.2 m away from the sample. An evacuated flight tube positioned in the path from the sample to the detector helped minimize photon scattering losses in the air. For such a photon-starving technique as nanoscale Bragg coherent diffractive imaging, the use of an evacuated flight tube, high sensor gain, and the detector's photon counting mode were essential. An Ultra-Violet laser of 375nm, guided via a confocal system available at the 34-IDC beamline, was focused down to 10 μm at a normal incidence to the isolated CBNO flake of interest. During the collection of rocking curves, the sample was continuously illuminated. A spatial light modulator (SLM) was employed to select the optical beam's topological charge, thereby controlling the OAM and torque transferred to the crystal (see Section **S6** and Figure **S3**, Supporting Information). Rocking curves were collected as a series of 2D diffraction patterns near the CBNO 002 Bragg peak, corresponding to $2\theta = 13.26°$, with a scanning range of $\Delta\theta = \pm 1.4°$ in the vicinity of the Bragg peak. A total of 360 patterns were gathered in a single rocking curve. The dataset for the virgin state (topological charge, $\ell = 0$) was obtained before cycling the CBNO crystal. The subsequent states under continuous $LG_\ell$ beam illumination, $\ell = 1$, $\ell = -1$ and $\ell = 0$ were recorded after 30 cycles of $\ell = 0$ illumination and release. This takes about 30 mins for one single 3D scan to be collected. Thus for all OAM applications $T = t_0 = t_1 = t_2 = t_3 = 30$ mins. This ensured that the system was entirely in equilibrium under laser illumination.

## Phase Retrieval Process

The collected 3D diffraction patterns were inverted from reciprocal into real space using iterative phase retrieval algorithms.[50] This gives us the complex wavefield post diffraction, which was given by $\rho(\mathbf{r}) = \rho_0(\mathbf{r})e^{(i\phi(\mathbf{r}))}$ where $\phi(\mathbf{r})$ is the phase and $\rho(r)$ is the amplitude of the wave. The phase carries the information of about the displacement field $u_{002}$, which could be determined by using $\phi(\mathbf{r}) = \mathbf{G_{002}}.\mathbf{u_{002}}(\mathbf{r})$. The shape and size of the nanocrystal were estimated from the reconstructed Bragg Electronic Density($\rho(\mathbf{r})$). For a given applied TL topological charge,

real-space images of the CBNO nanocrystal were reconstructed with approximately 33 nm spatial resolution as determined by the phase retrieval transfer function (PRTF) (see Figure **S28**, Supporting Information). The 3D nature of the reconstructed nanocrystal allowed to slice through the particle and analyze the different FE topologies. Fienup's hybrid input-output (HIO) approach was the basis for iterative phase retrieval techniques, which were further enhanced by randomized overrelaxation. When the measurement locations were close enough to one another to satisfy the oversampling criterion, an important stage in the process was to reverse the diffraction data using a computer algorithm. The first stage was to assume a 3D support volume where the sample density would be completely limited. These techniques impose a Fourier transform, both forward and backward, between the real and reciprocal spaces, imposing an intensity mask constraint in the former and a support constraint in the latter.

## Twisted-Light Raman Spectroscopy

A 532 nm wavelength light from the Witec Alpha 300R series was used to perform the Raman Measurements. The Witec Alpha 300R was modified with a free beam coupler to introduce the twisted light of wavelength 375 nm on to the sample surface. During the collection of a single spectrum, the sample was continuously illuminated. A spatial light modulator (SLM) was employed to select the optical beam's topological charge, thereby controlling the OAM and torque transferred to the crystal (see Section **S19** and Figure **S30**, Supporting Information). An Andor CCD was used to collect and count photons scattered from the CBNO nanoflake. A spectroscope grating of 1800 grmm$^{-1}$ was used to obtain a high-resolution spectrum of the sample under various topological charges. A Zeiss 100x microscope objective was used for focusing the laser beams onto the nanoflake as shown in Figure **S30** (Supporting Information). The integration time of 1 *s* was used to collect 100 accumulations of the spectrum to obtain a clean spectrum with a low signal-to-noise ratio. The reference spectrum was collected before cycling the system. The subsequent spectrums were collected under continuous illuminations of $\ell = 1$, $\ell = -1$ and $\ell = 0$ were collected. The experimental procedure is highlighted in Figure **S36** (Supporting Information).

## First-Principles Calculations

First-principles calculations were performed using the CASTEP (Cambridge Serial Total Energy Package)[54] and Quantum ESPRESSO (QE)[55] packages. The calculations involving the application of an external light beam carrying Orbital Angular Momentum (OAM) with different topological charges ($\ell$) were performed using CASTEP. The experimental electric field component of the OAM beam was explicitly included in these calculations. The Perdew-Burke-Ernzerhof (PBEsol) exchange-correlation functional within the generalized gradient approximation (GGA)[56] was employed for all calculations. Norm-conserving pseudopotentials and a plane-wave basis set with a kinetic energy cutoff of 600 eV were used. The pseudopotentials for Cs, Bi, Nb, and O were taken from the CASTEP library.

The Brillouin zone was sampled using a 6 × 6 × 6 Monkhorst-Pack grid.[57] The self-consistent field (SCF) calculations were converged to an energy threshold of $1 \times 10^{-6}$ eV. The initial molecular structure of CBNO was obtained from experimental theoretical data predictions

available on the Materials Project. The structures were optimized using density functional theory (DFT) as implemented in Quantum ESPRESSO. The Perdew-Burke-Ernzerhof (PBEsol) exchange-correlation function was chosen to describe the electron-electron interactions. The unit cell parameters are: $a$ = 11.87380 Å, $b$ = 5.45730 Å, $c$ = 5.55750 Å, with angles α = 90°, β = 90°, γ = 90°. Atomic positions were fully relaxed until the forces on each atom were less than 0.01 eVÅ$^{-1}$, and the stress tensor was below 1× 10$^{-3}$ GPa. The polarizability was computed using density functional perturbation theory (DFPT).[58] Infrared and Raman spectra were obtained by calculating the dynamical charges and the Raman tensors, respectively. The dielectric function and the Raman activities were computed to simulate the IR and Raman spectra.

# Acknowledgements

E.F. and M.N conceived the project and conceptualized the experiments. J.S. and J.J. grew and provided free-standing and epitaxial 2D CBNO samples. N.N, V.T, J.B, W.C,R.H., and E.F Performed the OAM BCDI measurements and characterization. BCDI analysis using phase retrieval algorithms was performed by N.N and E.F OAM Raman measurements and analysis was performed by N.N, V.T, P.B, A.N., M.N., and E.F., A.D performed the DFT computations. N.N and E.F. wrote the paper. All the authors discussed the results and commented on the manuscript. The authors thank S. Srinivasan(RPI) and J. Anderson(RPI) for her help with the Timed Raman Measurements and Thermal Raman Measurements. The authors thank S. Williams (RPI), A. Ndao (UCSD), L. Caretta (Brown University), and D. Kumah (Duke University) for the stimulating conversations on this manuscript. This work was supported by the US Department of Energy (DOE), Basic Energy Sciences, Materials Sciences and Engineering Division, under grant No. DE-SC0023148 (OBCDI technique, ORAMAN and analysis), and the US Department of Defense, Air Force Office of Scientific Research (AFOSR), under award No. FA9550-23-1-0325 (Program Manager: Dr. Ali Sayir) for work on probing topological vortices and piezoelectric enhancements. E.F. and M.N acknowledge support from the PAIR-UP Imaging supported by Gordon and Betty Moore Foundation. J.S. thanks the support from NSF under award number 2024972. This research used resources of the Advanced Photon Source (APS), a U.S. Department of Energy (DOE) Office of Science User Facility, operated for the DOE Office of Science by Argonne National Laboratory (ANL) under contract No. DE-AC02-06CH11357.

# Author Contributions

R.H., W.C., and E.F. designed and performed the BCDI experiment. J.J. and J.S. grew and provided the samples. V.T, P.B., and M.N synthesized the twisted beam.M.N and V.T acknowledged the support of The Office of Advanced Scientific Computing Research within the

Office of Science US Department of Energy (DOE) under grant No DE-SC0024676. All authors interpreted the results and contributed to writing the manuscript.

# Real-Time Tracking of Nanoscale Morphology and Strain Evolution in $Bi_2WO_6$ via Operando Coherent X-Ray Imaging

Jackson Anderson, Nimish P. Nazirkar, Atoumane Ndiaye, Julie Barringer, Viet Tran, Pascal Bassène, Wonsuk Cha, Jie Jiang, Jian Shi, Ross Harder, Moussa N'Gom, Edwin Fohtung
First published: 24 June 2025 **https://doi.org/10.1002/adma.202504445**

## Abstract

Nanostructuring photocatalytic and catalytic materials substantially increases the surface-to-volume ratio, thereby exposing a greater number of active sites essential for enhanced catalytic efficiency. However, optimizing these efficiencies requires the non-destructive, *operando* interrogation of individual nanocrystals under realistic catalytic conditions—a capability that has long remained elusive. Here, this challenge is addressed by reporting three-dimensional imaging of defects, crystal morphology, and strain dynamics in individual $Bi_2WO_6$ (BWO) nanoflakes using Bragg coherent diffractive imaging (BCDI) under *operando* temperature, gas, and light-driven conditions. It is demonstrated that maintaining a constant temperature of 40°C thermally activates charge carriers, likely enhancing their mobility and reducing recombination rates. Furthermore, an Argon (Ar) gas flow stabilizes the reaction environment, while a mixed Hydrogen–Nitrogen ($H_2$ + $N_2$) flow induces a hydrogen-triggered semiconducting-to-metallic (SM) electronic phase transition accompanied by a structural transformation, as supported by density functional theory (DFT) calculations. Both DFT and BCDI analyses reveal that during the SM phase transition, a new structural phase nucleates near defects and propagates inhomogeneously. Notably, the onset of nanoscale cracking is observed, driven by localized strain accumulation and environmental cycling, which increases surface area and potentially introduces new reactive sites. These findings illustrate that combining advanced nanostructuring with *operando* imaging techniques can provide critical insights into the local structural features that govern photocatalytic performance, paving the way for the rational design of next-generation photocatalytic materials.

# Graphical Abstract

Bragg Coherent Diffraction Imaging is used to study the structural behavior of a BWO nanoparticle as it is exposed to Argon and $H_2$ + $N_2$ gas environments. In the presence of the $H_2$ + $N_2$ gas, a semiconducting to metallic phase transition is observed to nucleate from dislocations running from the bulk to the surface.

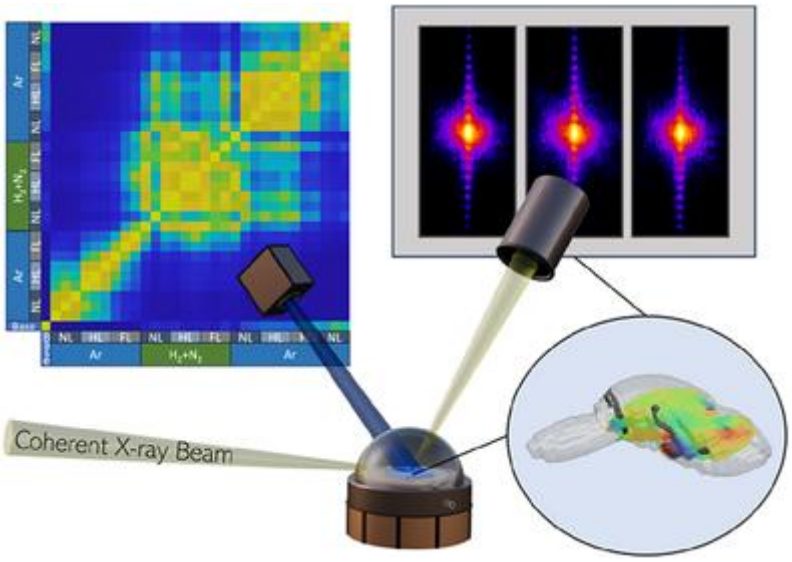


# 1 Introduction

Bismuth tungstate ($Bi_2WO_6$, BWO) has emerged as a significant material in photocatalysis due to its unique structural, electrical, photoluminescent, and photocatalytic properties.[1, 2] The material's photocatalytic efficiency is primarily attributed to its bandgap of approximately 2.8 eV, which allows for effective absorption of visible light, making it suitable for various photocatalytic applications, including water splitting and pollutant degradation.[3-5] The structural characteristics of BWO play a crucial role in its photocatalytic performance.[6-9] Research indicates that the synthesis method significantly influences the morphology and crystallinity of BWO, which in turn affects its photocatalytic activity.[5, 10-12] For instance, the solvothermal method has been shown to produce 2D BWO nanoplates with enhanced light absorption and redox properties, which are advantageous for photocatalytic applications.[13] Furthermore, modifications such as doping with metals or the incorporation of composites (e.g., graphene) have been explored to improve charge separation and enhance photocatalytic efficiency.[3, 14-16] These modifications can lead to improved electron mobility and reduced recombination rates of photogenerated charge carriers, which are critical for effective photocatalysis.[17] The photoluminescent properties of BWO also contribute to its photocatalytic capabilities. The material exhibits strong photoluminescence,[4, 18, 19] which is indicative of efficient charge separation and transfer processes. Studies have shown that the introduction of defects or dopants can further enhance these properties, leading to improved photocatalytic performance under visible light irradiation.[4, 20-23] Additionally, the hierarchical structure of BWO,

such as microballs or nanosheets, has been associated with increased surface area and active sites for photocatalytic reactions, thereby enhancing its overall activity.[3, 13]

Despite these efforts, current state-of-the-art characterizations are not capable of probing and distinguishing defects types, layer morphology, crystal facets, and lattice strain under operando conditions with high spatio-temporal resolution. In this study, we aim to address these challenges by exploring the strain dynamics, defect behavior, facet types, and phase transformations in nanostructured BWO nanoflakes under operando conditions using Bragg coherent diffractive imaging (BCDI).[24-31] By varying temperature, gas environment, and light irradiation, we seek to understand their effects on the photocatalytic activity of BWO. Additionally, DFT calculations will support our experimental findings, providing a comprehensive understanding of the underlying mechanisms. This research will contribute to the rational design and improvement of nanostructured photocatalytic materials.

# 2 Results and Discussion

## 2.1 Experiment

We collected coherent BWO (113) ($2\theta$ = 23.3°) diffraction data at a constant temperature of 40° C for a single nanoparticle while varying gas environment and light level exposure.

Scans were conducted with incident angle $\phi$ = ±0.6° with an angular step size of 0.01° around the BWO (113) Bragg peak to capture the 3D reciprocal space intensity profile. The baseline state of the crystal was characterized by scanning in the ground state of 40 °C, without light and in an air environment. Argon was then pumped into the chamber and the system was given one hour to reach equilibrium. Three light levels were then tested: No Light (NL), Half Light (HL), and Full Light (FL). These light levels were given by the settings in the LED light source used (SugarCUBE Blue LED), and correspond to 0, 420, and 780 mW respectively. The experimental setup prevented the exact power output onto the sample from being measured directly, therefore the listed values in mW are estimates based on the total LED output and the transmission rates of the optical setup used to focus the LED onto the sample. Three scans were recorded at each light level, and the system was given 5 min after changing light levels to stabilize. The environment was then changed to a $H_2$ + $N_2$ mixture and the data was collected in the same way. The system then returned to an Ar environment and scans were conducted at each of the light levels again, with the addition of three NL scans taken at the end of the cycle. A summary of the collected diffraction data can be found in Figure **S1** (Supporting Information).

## 2.2 Operando Analysis of Structural and Electronic Evolution

In our BCDI operando (temperature, gas component, and laser fluence) measurements, we analyzed changes in morphology, the symmetry of diffraction patterns, speckle sizes, intensity variations, and diffused scattering clouds near the (113) reciprocal lattice point under operando

conditions. The observed fringe oscillations (see **Figure 1c**) typically arise from a convolution of scattering effects due to the finite size of the BWO crystal facet and lattice distortions.[25, 26]

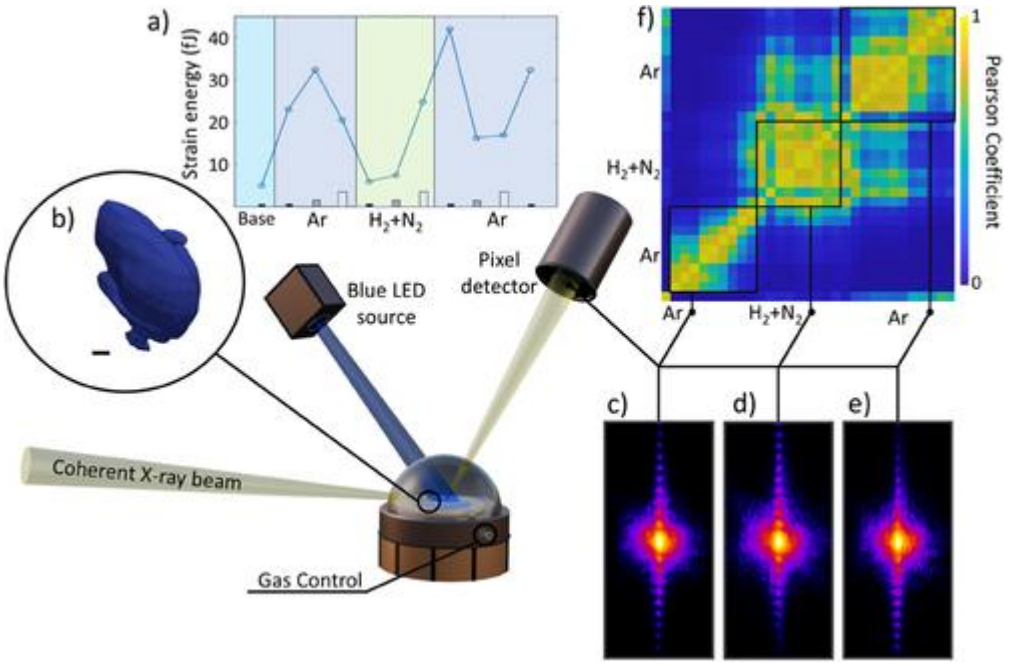


**Figure 1**
**Open in figure viewerPowerPoint**
An overview of the experimental setup and method. a) Plot of the surface strain energy of the particle in response to the gas environment and light level. b) Reconstruction of the particle from diffraction data, scale bar is 100 nm. c–e) Diffraction patterns (integrated across full rocking curve) as collected by pixel detector for the three gas environment (Ar, H, and Ar respectively) all at no light applied and f) the Pearson correlation matrix of the central intensity region of the diffraction patterns for all environments and light levels.

The diffraction data confirm that these oscillations correspond to the (113) facets. While the intensity symmetry of the fringes varies—indicative of significant strain within the NP—the fringe spacing remains constant, suggesting that the width of the diffracting sample in the [113] direction remains relatively fixed. The central intensity regions of the diffraction pattern fluctuate significantly between scans, correlating with structural and morphological changes within the NP volume.

To quantify these variations, a Pearson correlation analysis was performed on the central intensity region of the diffraction patterns (see **Figure 2**). The correlation coefficients between each pair of patterns reveal that the base scan is largely uncorrelated with scans conducted in the gas environment, indicating substantial structural and/or morphological changes. A mechanism for these transformations, along with an analysis of strain evolution, is discussed below.

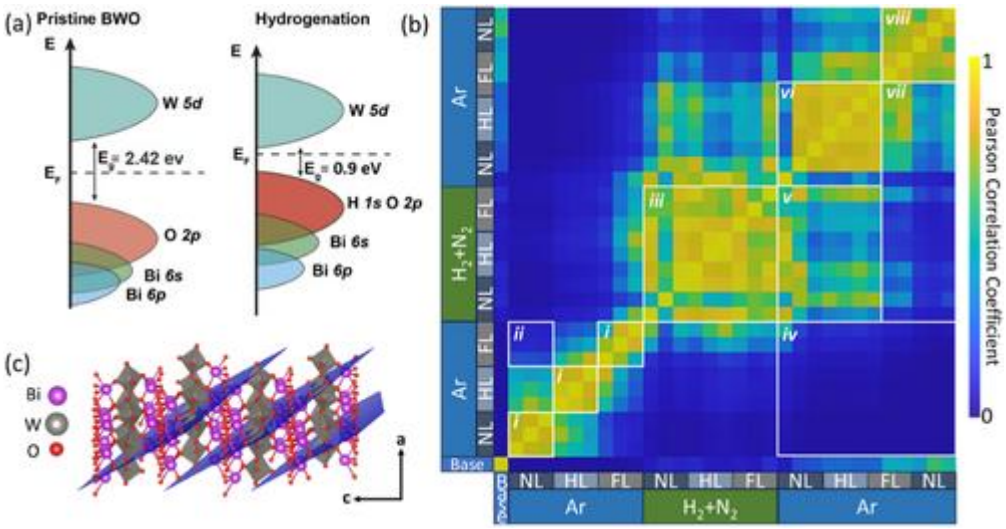


**Figure 2**

**Open in figure viewerPowerPoint**

a) A schematic representation of simulated band structure diagram and how it changes in response to the gas environment. b) The full Pearson correlation matrix for all collected diffraction data. Each colored pixel of the image represents the Pearson correlation coefficient between the two diffraction datasets in the corresponding row and column, with the color indicating the value of the coefficient (ranging from 0 to 1). Diffractions are organized chronologically along the axes, broken up by gas environment and light level: No light (NL), Half intensity/Light (HL) and Full intensity/Light (FL). Regions of interest are marked with white boxes and labeled (*i-viii*). c) A rendered[32] 2x2x2 BWO supercell with (113) planes drawn in blue.

## 2.3 Environmental Effects and the Semiconductor-to-Metallic Transition

Scans conducted under the same light level and gas environment show high correlation, indicating structural stability under fixed conditions. However, when initially exposed to Argon, the system responds strongly to changes in light intensity (see Figure **2b**-*i*), as evidenced by lower correlation between scans taken at different light levels (see Figure **2b**-*ii*). This behavior aligns with expectations for a semiconductor. In contrast, during exposure to hydrogen, diffraction patterns remain more uniformly correlated (see Figure **2b**-*iii*), suggesting reduced sensitivity to light—a characteristic more typical of a metallic state. This observation suggest a semiconducting-to-metallic (SM) phase transition induced by hydrogen.

Hydrogen is a well-known reducing agent that can modulate the electronic properties of oxide materials by introducing an abundance of charge carriers, effectively lowering the bandgap.[33-37] To probe the effect of hydrogen exposure computationally, we simulated hydrogenation using both periodic (CASTEP) and non- periodic ($DMol^3$) frameworks. We employed $DMol^3$, a density functional theory (DFT) software,[38, 39] to model a BWO unit cell on the crystal surface as an isolated cluster using non-periodic boundary conditions to see how the system responded to the introduction of hydrogen and nitrogen atoms. This gave us a stable configuration, on

which we performed DFT simulations of hydrogen interactions with oxygen active sites. The results show a substantial band gap reduction, from 2.42 eV in the simulated base state to 0.9 eV in the presence of hydrogen (Figure **2a**). While the absolute band gap in the base state is slightly lower than experimental values (2.6–2.8 eV)—a known trend in DFT calculations[40]—the significant reduction due to hydrogen adsorption is evident. This reduction arises from strong hybridization between hydrogen-induced states and the conduction band, leading to charge delocalization. Nitrogen was found to not interact directly with the BWO lattice, instead only bonding to hydrogen atoms already attached at active sites. We can use this non-periodic surface calculation to inform a calculation of BWO crystal completely saturated with hydrogen. Under periodic boundary conditions (CASTEP calculations), translational symmetry enhances band dispersion, fully closing the bandgap and inducing a metallic state. The excess charge carriers generated by hydrogen interactions saturate pristine state, leading to a full semiconductor to metallic transition. Strain and shear stress also plays a minor role in bandgap dynamics, with calculations showing a slight decrease of roughly 0.36 eV (see Figure **S2**, Supporting Information) under observed stresses (Table **S1**, Supporting Information). However, hydrogenation is the main cause of the phase transition. Further details of the DFT calculations can be found in Supporting Information (Figures **S3–S5**).

## 2.4 Photo-Activation and Charge Carrier Effects

From the low correlation between the two Argon data sets (see Figure **2b**-*iv*), it is clear that the system does not revert to its original state upon reintroduction to the Argon environment. Instead, the sample retains a high correlation with the previously induced hydrogen phase (see Figure **2b**-*v*), exhibiting a similar insensitivity to light (see Figure **2b**-*vi*) until full-intensity light exposure is applied, at which point the correlation sharply decreases (see Figure **2b**-*vii*). This suggests a photo-activated or photocatalytic process that drives the system into a new state (see Figure **2b**-*viii*).

$Bi_2WO_6$ is known to facilitate $N_2$ reduction reactions $N_2 \rightarrow NH_3$ through photo-activated charge separation at metallic Bi and defect sites.[41] It is therefore plausible that residual nitrogen and hydrogen undergo activation and react under full light (FL) exposure. Typical $N_2$ reduction experiments use sacrificial hole scavengers like methanol to mitigate the accumulation of holes in the valence band, scavengers which were absent in our experimental conditions.[41] The resulting excess holes could explain the drop in correlation observed in the final NL diffraction patterns, as they likely induce large strain effects and increase defect density.

The combined structural, diffraction, and computational analyses highlight the critical role of facet-dependent charge carrier dynamics and environmental interactions in tuning the electronic and photocatalytic behavior of BWO. The observed hydrogen-induced SM phase transition and subsequent photo-driven restructuring suggest new pathways for designing tunable, light-responsive photocatalysts. By leveraging operando BCDI to track nanoscale strain and facet evolution, these findings provide insight into defect migration, charge separation efficiency, and potential catalytic enhancements under real operating conditions.

## 2.5 Nanoscale Structure from BCDI

In our BCDI experimenent, the measured intensity is given by:

(1)

Using iterative phase retrieval alogorithms,[26, 42] a 3D reconstruction of a single BWO nanocrystal is produced from the measured intensities collected from the (113) Bragg peaks using coherent X-ray diffraction. This reconstruction complex Bragg electronic density consists of both an amplitude, , and a phase, $\mathbf{G}_{113} \cdot \mathbf{u}(\mathbf{r})$, of the X-ray complex wave field. The amplitude represents the crystal's Bragg electron density, while the phase encodes the projection of the atomic displacement field, $u_{113}$, along the reciprocal lattice vector $\mathbf{G}_{113}$.

The coordinate system for the reconstructions is defined such that the *z*-axis is aligned with the (113) plane normals; consequently, taking the derivative yields the out-of-plane strain components.

**Figure 3** shows cross sections from reconstructions of the base state and the first no-light Argon measurement. A full comparison of reconstructed particle isosurfaces can be found in Figure **S6** (Supporting Information), along with a discussion of the facet morphology. In the base state (Figure **3a,c**), the circled feature is characteristic of an intrinsic defect structure within the NP. Phase wraps and high strain boundaries—especially when accompanied by amplitude singularities, as illustrated in **Figure 4**—indicate local high strain regions where the particle is heavily displaced away from the Bragg condition due to defects such as dislocations.[44] In contrast, the reconstructions from the Argon environment (Figure **3b,d**) reveal that this defect feature is largely absent from the bulk, with a high-strain region emerging near the surface. We therefore observe that exposure to an Argon environment reduces the presence of bulk defects. In $Bi_2WO_6$ (BWO), such defects are commonly associated with catalytically active sites, as they can lower the effective bandgap and prolong charge separation.[45] The structure of BWO, which exhibits large channel-like voids between the $[WO_4]^{-2}$ octahedra and the $[Bi_2O_2]^{+2}$ layers (Figure **4a**), may promote diffusion pathways.[46] Hydrogen readily bonds with oxygen active sites in BWO, leading to a reduction in the electronic band gap as demonstrated by density functional theory simulations (see Figures **S2–S5**, Supporting Information). The resulting local strain may be relieved by the formation of dislocations, which in turn provide additional access channels for gas infiltration, facilitate further hydrogen bonding, and nucleate metallic phase domains.

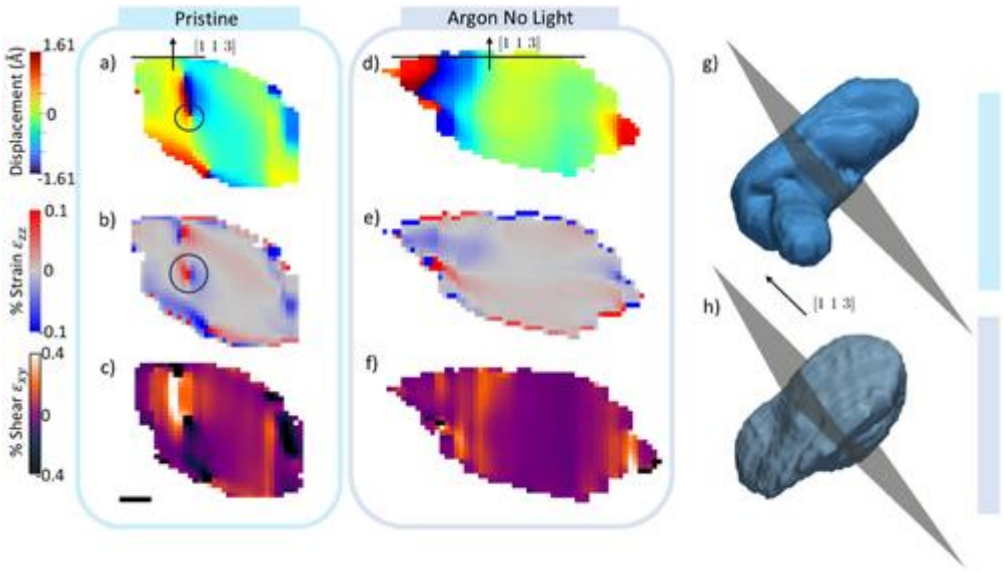


**Figure 3**

**Open in figure viewerPowerPoint**

Strain evolution and morphology of nanoparticle. A comparison of the reconstructed particle in the base environment vs argon environment with no applied light. a–c) Slices through the reconstructed volume showing the displacement field, out-of-plane strain, and in-plane strain for the pristine state, respectively. d–f) show the same for the argon no light state. g–h) Isosurfaces of the reconstructed particle provide context for the shape and position of the slice for the pristine and argon-exposed particles, respectively. Scale bar in the bottom left is 50 nm. The circled region in (a) and (b) highlights a reconstructed feature characteristic of a defect. A noticeable morphological difference between the pristine and argon-exposed states is visible in panels (g) and (h), suggesting the possible onset of cracking or decoherence. This feature, though subtle in strain maps, may be indicative of light- or gas-environment-induced loss of crystallographic continuity. The emergence of such morphological detachment, paired with surface-localized strain, supports the interpretation of a possible early-stage cracking process.

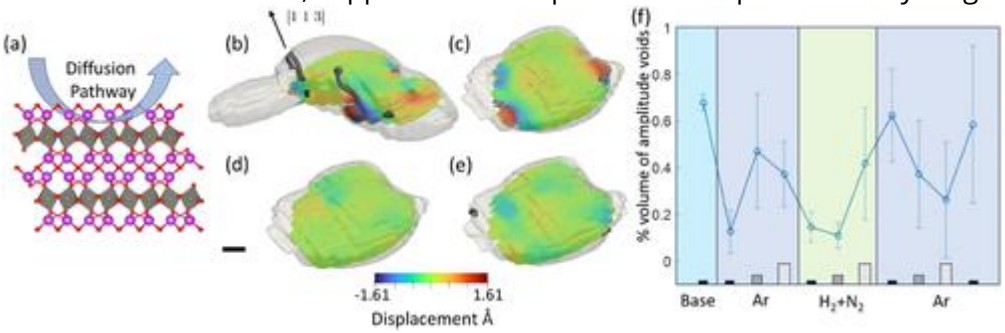


**Figure 4**

**Open in figure viewerPowerPoint**

Defect and cracking-like morphology tracking in reconstructed BWO particles. a) A schematic of the BWO supercell viewed along the [100] direction, highlighting potential diffusion pathways formed by extended structural gaps. b–e) 3D reconstructions of a representative particle: (b) in the base environment, and c–e) in an argon atmosphere without applied light. Dislocation regions, identified by tracking singularities in the complex Bragg electronic densities—

specifically in the displacement field and amplitude—are shown as gray isosurfaces. See Section **S3** and Figure **S7** (Supporting Information) for additional details. Internal slices are colored by atomic displacement magnitude along the [113] crystallographic direction. Scale bar in (d) represents 50 nm. f) Volume fraction of the particle identified as dislocation-rich, shown as a function of gas environment and light exposure. Background shading denotes the gas environment (Base, Ar, $H_2$+$N_2$, Ar), and color bars beneath each point indicate light intensity (NL = no light, HL = high light, FL = full light). Each data point represents the mean from three independent reconstructions; error bars combine the standard error of the mean with reconstruction uncertainties. We note that in panels (c–e), a morphological change is observed where a portion of the particle appears partially decoupled from the rest of the crystalline volume. This detachment may reflect a cracking-like event or a loss of lattice coherence. While no sharp discontinuity is observed in the strain slices, the interface appears diffuse, suggesting a relaxation mechanism rather than brittle fracture. Such features may have implications for long-term structural stability and catalytic performance. The observed changes, particularly under repeated Ar exposure, align with patterns reported for nanoscale crack formation[43] in perovskites under environmental cycling.

We hypothesize that the Argon environment applies a partial pressure on the residual reactants at these active sites, thereby encouraging diffusion toward the surface. The evolution of these defects in the no-light Argon environment is tracked in Figure **4**. The sequence in Figure **4b–e**, presented in chronological order, shows a drastic decrease in defects from the base state to the Argon environment, with a continued reduction under prolonged Argon exposure as dislocations migrate to the particle surface, annihilating and leaving behind slip or ledge features. These features would increase surface roughness, which could be a contribution to the large changes in NP shape we observed (see Figures **3** and **4**; Figure **S6**, Supporting Information). Redistributing bulk and surface strains could lead to crystal domain distortion and eventually particle cracking.[43] It is very likely cracking caused the disappearance of the cylindrical outcrop feature seen in the base state (Figure **4b**). Large scale changes like this to surface structure during gas cycling would greatly affect catalytic properties over time. Additional renders of Figure **4b** can be found in Figure **S8** (Supporting Information), which give better visualization of the 3D nature of the dislocations and initial particle shape.

The percent volume of local high strain regions (e.g., dislocations) within the NP is used as a quantitative measure of defect density. A radial plot of the displacement field surrounding the large dislocation core shown in Figure **4b** and fitting revealed it to be a mixed dislocation with a Burgers vector of 2.7Å (See Section **S3** and Figure **S7**, Supporting Information). Dislocation volume was identified as the high local strain regions surrounding displacements matching the Burgers vector magnitude. While the uncertainty from reconstruction and large fluctuations in observed defect volume between even scans with similar experimental conditions (see Figure **S9**, Supporting Information) produced larger error bars, several general trends can still be observed with confidence. After the initial decrease in the Argon environment, light exposure results in an increase in these dislocation regions. This behavior is expected for a photocatalytic material like BWO, as light stimulus promotes electron–hole separation, and the increased charge carrier density can induce strain fields that further deform active site regions. Moreover, due to the absence of methanol or a similar electron donor in our experiments, any

$N_2$ reduction reactions would generate a surplus of holes in the valence band, potentially leading to additional defect formation.[41] This mechanism could explain the hightened defect volume observed in the final Argon measurements.

## 2.6 Quantitative Strain Analysis and Kinetic Correlations

To quantitatively describe the strain trends within the NP, we performed a statistical analysis of the reconstructed strain, as presented in **Figure 5**. Across all gas environments, the mean strain in both the bulk and surface regions is slightly compressive relative to the base state but remains near zero overall, indicating a balance between compressive and tensile strains. This observation is reinforced by the symmetrical nature of the strain histograms. The root-mean-square (rms) strain in the bulk mirrors the trends observed in the defect volume (Figure **4**), confirming that these defects are the dominant source of strain within the NP. Bulk shear values can be found in Table **S1** (Supporting Information), which follow a similar trend to the strain data, supporting the defect migration hypothesis. The histograms further reveal an increased number of reconstructed regions with reconstructed strain values near ±1%, highlighting these high-strain singularities.

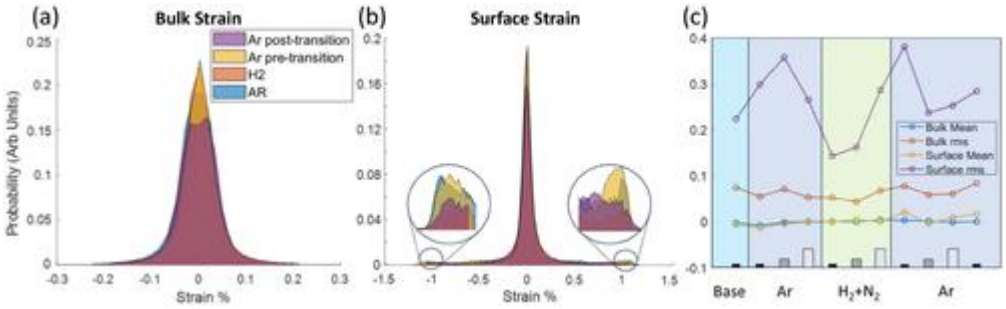


**Figure 5**

**Open in figure viewerPowerPoint**

Statistical analysis of the reconstructed strain. a,b) Strain distribution graphs of the particle strain values, separated by bulk and by surface. The pre- and post-transition labels in the legend relate to the feature observed in Figure **2b**-vii between the first and last two light levels in the second Argon exposure. The circled features in (b) show a 10x zoom in on the corresponding section of the graph. c) A graph of the mean and root mean squared (rms) strain separated by bulk and surface of the particle. Regions of the graph are colored by gas environment, and the color bars beneath each data point indicate the exposed light intensity (NL, HL, FL). Each data point is the average value from the three scans collected at each light level.

Notably, the rms surface strain deviates from the defect volume trends, increasing greatly in the first argon scans while defect volume decrease. We hypothesize that the argon environment creates a partial pressure on the chemical defects, such as oxygen vacancies. These defects then migrate to the surface of the crystal and are released, leaving behind a slip or a ledge on the surface, greatly increasing both compressive and tensile surface strains. A large increase in rms surface strains is observed, however it is somewhat difficult to differentiate the strain due to this redistribution caused by bulk defect migration from strain

due to gas adsorption. The surface strains are observed to be closely balanced between tensile and compressive, as seen in Figure **5b**, which results in a mostly constant and slightly compressive mean surface strain (Figure **5c**). This slight overall compressive strain observed across the majority of scans is likely the result of gas adsorption. Since the experiment was carried out a constant pressure, we must assume that large changes in the surface strain are mainly the result of bulk strain redistribution.

To connect these structural insights with the photocatalytic performance, we consider several kinetic models.

The Arrhenius[47] equation, , relates the reaction rate constant $k$ to the absolute temperature $T$, where $A$ is the pre-exponential factor, $E_a$ is the activation energy, and $R$ is the gas constant. Our experiments at room temperature and 40°C demonstrate enhanced defect activity and changes in strain evolution at elevated temperatures. By correlating these structural changes observed via BCDI with complementary measurements of reaction rates or charge carrier dynamics, an Arrhenius plot (i.e., ln $k$ versus $1/T$) can be constructed to extract $E_a$. This analysis can help to provide quantitative insight into the energy barriers for thermally activated processes within the NP. However, the scope of this article was focused on experimentally resolving the strains and defects.

To understand surface strains, defects and surface-mediated reactions in photocatalysis the Langmuir–Hinshelwood model can be used. Where $r$ is the reaction rate, $C$ is the reactant concentration, $K$ is the adsorption equilibrium constant, and $k$ is the rate constant for the surface reaction. Our BCDI data reveal that defect-rich regions, which serve as potential adsorption sites, can influence the local surface reactivity. By correlating the spatial distribution of defects (and the associated strain fields) with catalytic performance measurements, future experiments will help us to infer how variations in $K$ affect the overall photocatalytic activity.

Defects and strain also play a critical role in the recombination of photogenerated electron–hole pairs. Dislocations that migrate to the surface will leave slips or ledges behind. These lead to surface roughening, which can potentially enhance catalysis. Defects and strain both play a key role in band dynamics and charge separation, an important property for photocatalytic efficiency. Although BCDI does not directly measure carrier densities, the spatial maps of strain and defects serve as proxies for regions of enhanced recombination. By comparing these maps with independent measurements of carrier lifetimes, we can potentially correlate areas with high defect density from BCDI experiments to higher recombinationrates.

## 2.7 Stress-Induced Morphological Evolution and Cracking Behavior

Our high-resolution BCDI reconstructions (Figures **3** and **4**, and Figure **S6**, Supporting Information) reveal notable morphological and structural changes in BWO nanoparticles as a function of gas environment and light exposure. After being subjected to sequential Ar and $H_2$+$N_2$ exposure, the particle shows pronounced fragmentation and detachment of outer

volumes from the crystalline core. These morphological changes, especially evident in Figure **4(c–e)** and Figure **S6b–d** (Supporting Information), suggest a progressive loss of lattice coherence consistent with the onset of nanoscale cracking. This interpretation is further substantiated by strain mapping and statistical metrics. In Figure **5c**, both the mean and RMS strain in the *surface* region significantly exceed those in the bulk, suggesting that stress accumulates at the surface, potentially initiating de-cohesion. Complementary shear stress data (Table **S1**, Supporting Information) show large fluctuations in minimum and maximum stress values across the particle, with particularly negative mean stresses under Ar NL and HL conditions (e.g., $-3.33 \times 10^{-5}$ GPa for Ar NL). Such compressive shear stress could promote surface delamination or fracture under continued cycling.[43] Although cracking is traditionally viewed as a failure mode, we posit that in this context it may provide beneficial effects for photocatalysis. The increased surface area generated by crack propagation can expose previously inaccessible active sites, enhancing photocatalytic efficiency. Observed detachment of surface volumes (Figure **3g,h**) also suggests pathways for improved gas and reactant diffusion along internal interfaces formed post-crack. Additionally, mild decoherence and lattice distortions may result in local band structure changes (strain-induced shifts, see Figure **S2**, Supporting Information) that favor charge separation and reduce recombination, potentially improving photocatalytic turnover. Further work integrating electronic structure modeling and in situ performance measurements could help elucidate the precise catalytic consequences of these structural transitions.

# 3 Conclusion

We use BCDI and coherent diffraction analysis to track the defect structure of BWO flakes as they are exposed to differing gas environments and light levels. Phase retrieval techniques allow us to characterize the defect concentration by tracking regions of low reconstructed amplitude, as well as the strain fields throughout the sample. These defect regions, and the strain fields they produce, play a key role in the overall structure of and strain within the crystal. We observe a marked change in structure and response to light when the sample is exposed to a mixed $H_2$ + $N_2$ environment, indicating a semiconducting to metallic phase transition, a conclusion which is confirmed by DFT simulation. The crystal stays in this metallic phase despite a return to a pure argon environment until exposed to intense light, at which point a photocatalytic process occurs causing the concentration of defects to increase dramatically and the sample to begin transitioning to a new phase. Importantly, under specific gas exposures and thermal-light cycling, we also observe surface-localized morphological changes consistent with the onset of nanoscale cracking. This conclusion is supported by increased strain localization near the surface, fragmentation of isosurfaces, and significant changes in displacement gradients. While traditionally considered detrimental, we propose that controlled, stress-induced cracking may be beneficial for photocatalysis, as it enhances surface area, exposes buried reactive sites, and introduces strain-driven band modifications favorable for carrier separation.

Our results showcase the strength of BCDI as a non-invasive tool for characterizing the strain states within photocatalytic materials, which can prove useful for operando study of future

material design. The operando BCDI results, combined with theoretical computations and a detailed kinetic analysis, offer deep insight into the evolution of defect structures, strain, and cracking within photocatalytic materials such as BWO nanoflakes under various environmental conditions. These findings not only advance our understanding of the fundamental processes governing photocatalysis, but also provide a pathway for the rational design of nanostructured photocatalytic materials with improved performance, potentially leveraging strain and fracture as active tuning mechanisms.

# 4 Experimental Section

## Sample Preparation

BWO nanoflakes were fabricated by exfoliation from a bulk crystal. The bulk crystal was synthesized using a flux growth method with $Li_2B_4O_7$ as the flux. $Bi_2O_3$ (99.9%), $WO_3$ (99.9%), and $Li_2B_4O_7$ (99.9%) powders were mixed in a molar ratio of 3:3:7. The mixture was heated to 1000 °C and held for 10 h to form a uniform solution. The solution was then cooled to 940 °C at a rate of 10 °C/h, followed by a slower cooling to 840 °C at 1 °C/h. Finally, the solution was allowed to cool naturally to room temperature. BWO single crystals with sizes ranging from 1 to 5 mm were obtained after the flux was removed by treatment with hot nitric acid. The BWO nanoflakes were then exfoliated and transferred onto a substrate using polydimethylsiloxane (PDMS).

## BCDI Experimental Details

BCDI experiments for BWO were conducted at the 34-ID-C beamline, APS (ANL, USA). Using focused coherent X-ray (0.7 × 0.7 $\mu m^2$) by the KB-mirror with 9.0 keV photon energy, we measured CXD patterns in the vicinity of the BWO (113) Bragg peak. Each CXD pattern was collected by a 2D X-ray detector (Medipix2 CMOS with 55 μm pixel size) positioned 0.75m from the sample stage, with the rotation of the BWO crystal on the goniometer along the rocking curve. To facilitate high spatial resolution, a wide range (−0.6° to 0.6°) of rocking scans with a step size of 0.01° was measured. The sample was mounted in a small flow cell equipped with a sample heater kept at a constant 40° C (See Section **S2**, Supporting Information, for a discussion of why this temperature was chosen). Gas environment was controlled by flowing pure Argon or hydrogen-nitrogen mixtures through the cell at a fixed flow rate of 190 mL/min. The sample was stimulated with light by a SugarCUBE Blue LED (458nm) guided into the 1/4 inch beam-line microscope input using fiber optic cable, with an estimated transmission rate of 70%. The LED power was measured using a S121C sensor with 9.5mm diameter, and the power density of the HL and FL states was determined to be 1.9 and 3.53 $W/cm^2$ respectively. Given the size of the microscope input and the fiber optic transmission rate, we estimate the NP was exposed to 420 and 780mW respectively.

## Phase Retrieval Process

In total, 10 consecutive scans of the same BWO flake were accumulated to enhance the signal-to-noise ratio. To manage the excessive oversampling of the reciprocal space's coherent interference patterns—due to the extended sample-to-detector distance—the summed diffraction pattern was typically binned (2 by 2). The phase-retrieval process[42] was performed using combinations of the ER and HIO algorithms (200:50), with a total of 250 iterations. A cubic initial support with a random phase was used. Consistent results were achieved across all reconstruction trials. Analysis using Phase Retrieval Transfer Function reports an average error of 1.2% and a spatial resolution of 20nm (see Figure **S10**, Supporting Information). NP shape was defined using the converged support, which contains all the finite reconstructed amplitudes. The Surface was then defined to be the first 30 nm penetrating into the NP.

### Computational Details

Density Functional Theory (DFT) calculations were performed using the CASTEP code[48] with periodic boundary conditions to investigate interactions between $Bi_2WO_6$ (BWO) and hydrogen or argon gases, focusing on the effects at oxygen active sites within the unit cell. The Perdew-Burke-Ernzerhof (PBE) exchange-correlation functional[49] was employed within the generalized gradient approximation (GGA) to obtain optimized structural and electronic properties. To improve the accuracy of the band gap, a Hubbard U correction was applied to the W-5*d* orbitals, with the U value optimized based on prior studies.

A plane-wave cutoff energy of 600 eV and a Monkhorst-Pack k-point grid[50] of 5 × 5 × 5 were selected to ensure convergence in total energy and charge density. Structural relaxation was performed until atomic forces were minimized below 0.01 eV/Å, ensuring stability in the optimized configurations.

To simulate hydrogen interaction, hydrogen atoms were introduced at a ratio of 4:1 per unit cell relative to oxygen sites, allowing full structural relaxations to identify the most energetically favorable configurations. This interaction led to a significant reduction in the bandgap from 2.4 eV in pristine BWO to a metallic state due to strong hybridization between hydrogen-induced states and the conduction band.

In contrast, argon gas was introduced to assess its role as an inert stabilizer. Computational results confirmed that argon does not chemically bond with BWO but rather facilitates a “reset” effect by reversing hydrogen-induced structural and electronic modifications. This process restores the band gap to 2.18 eV, transitioning BWO from a metallic back to a semiconducting state without introducing additional chemical interactions. This stabilization mechanism allows for controlled cycling between different electronic phases while preserving structural integrity.

All calculations were performed at zero temperature, with extrapolations to elevated temperatures guided by empirical observations of BWO—s behavior under different gas environments.

# Acknowledgements

This work was supported by the US Department of Energy (DOE), Basic Energy Sciences, Materials Sciences and Engineering Division, under grant No. DE-SC0023148 (BCDI technique development), and the US Department of Defense, Air Force Office of Scientific Research (AFOSR), under award No. FA9550-23-1-0325 (Program Manager: Dr. Ali Sayir) for work on defects structure. M.N and V.T acknowledge the support of The Office of Advanced Scientific Computing Research within the Office of Science US Department of Energy (DOE) under grant No DE-SC0024676. J.S. and E.F. thanks the support from NSF under award number 2024972. A.N., M.N'G., and E.F., acknowledge support from the Gordon and Betty Moore Foundation for the PAIR UP Imaging Science Program.This work was supported in part by the Empire State Development's Division of Science, Technology and Innovation (NYSTAR) Focus Center at RPI, C210117 (J.S.). (J.S.) also thanks support from US NSF under award No. 2314614. This research used resources of the Advanced Photon Source (APS), a U.S. Department of Energy (DOE) Office of Science User Facility, operated for the DOE Office of Science by Argonne National Laboratory (ANL) under contract No. DE-AC02-06CH11357.

# Author Contributions

M.N. and E.F. conceived the project and conceptualized the experiments. R.H., W.C., and E.F. designed and performed the BCDI experiments. J.S. and J.J. grew and provided the BWO 2D samples. J.A., V.T., P.B., and M. N. developed the LED system. J.A., N.N., J.B., W.C., R.H., and E.F. performed the operando BCDI measurements and characterization. BCDI analysis using phase retrieval algorithms was performed by J.A., N.N., J.B., and E.F. A.D. performed the DFT computations. J.A. and E.F. wrote the paper. All authors discussed the results and commented on the manuscript.